

This is to certify that the

thesis entitled

**A CROSS SECTION ANALYSIS FINITE ELEMENT CODE FOR TUBE
HYDROFORMING**

presented by


Yabo Guan

has been accepted towards fulfillment
of the requirements for

Masters

Mechanical Engineering

_____ degree in _____



Major professor

Date 12/11/2000



PLACE IN RETURN BOX to remove this checkout from your record.
TO AVOID FINES return on or before date due.
MAY BE RECALLED with earlier due date if requested.

DATE DUE	DATE DUE	DATE DUE

**A CROSS SECTION ANALYSIS FINITE ELEMENT CODE
FOR TUBE HYDROFORMING**

By

Yabo Guan

A THESIS

**Submitted to
Michigan State University
In partial fulfillment of the requirements
For the degree of**

MASTER OF SCIENCE

Department of Mechanical Engineering

2000

ABSTRACT

A CROSS SECTION ANALYSIS FINITE ELEMENT CODE FOR TUBE HYDROFORMING

By

Yabo Guan

Hydroforming of metal components is widely used in several industries. While numerous variations of hydroforming exist, the basic principle remains the same: utilize fluid pressure to form a component. In tube hydroforming, internal pressure is applied to form a tubular metal blank into a structural component having a closed cross section.

The thesis presents a "cross-section" analysis method for calculating tube stretching and bending followed by hydroforming and expansion to fill the die in the hydroforming process. The material is assumed to be elastic-plastic and to satisfy the plasticity model that takes into account rate-independent, work hardening and normal anisotropy. Based on the virtual work principle and constitutive equation, the equilibrium equation can be derived. Numerical solution obtained from a Total-Lagrangian formulation of a general shell theory is employed. The boundary friction condition is introduced into the formulation in the form of penalty function, which imposes the constraints directly into the tangent stiffness matrix. The Newton-Raphson algorithm is used to solve the nonlinear equation.

ACKNOWLEDGMENTS

The author wishes to express his appreciation to the following people and institutions for making the completion of his Master of Science possible.

To my major professor, Dr. Farhang Pourboghraat, for his help, patience and guidance, without which this project would not have been possible.

To Ford Company and MSU Manufacturing Research Consortium, for their financial support of my master studies.

To Haiyan Miao, my wife and closest friend, for her support and encouragement, when I need it most, and for help in preparing this manuscript.

TABLE OF CONTENTS

ACKNOWLEDGMENTS.....	iii
LIST OF CONTENTS.....	iv
LIST OF FIGURES.....	vi
INTRODUCTION.....	1
CHAPTER 1	
LITERATURE REIVEW.....	4
CHAPTER 2	
THIN SHELL THEORY.....	8
Principal Stretch (Total Lagrangian).....	8
Principal Curvature and Stretch (Updated Lagrangian).....	11
CHAPTER 3	
KINEMATICS.....	15
Straight Segment.....	16
Circular Arc Segment.....	17
Constraints.....	20
CHAPTER 4	
CONSTITUTIVE EQUATION.....	21
CHAPTER 5	
CONTACT ALGORITHM.....	23
Numerical Procedures for Contact.....	23
Detection of Contact.....	25
Contact Tolerance.....	25
Normal Vector and Tangential Vector.....	26
Condition for Contact Violation.....	28
The Projection Algorithm.....	29
The Iterative Method.....	30
The Directive Method.....	30
Implementation of Constraint.....	31
Friction Model.....	32
Separation.....	34
CHAPTER 6	
NUMERICAL SIMULATION.....	35
Principle of Virtual Work.....	35
Newton-Raphson Algorithm.....	36

Three Types of Modeling.....	37
Tube Bending Modeling.....	37
Pressure Loading Modeling.....	39
Frictional Contact Modeling.....	40
CHAPTER 7	
PROGRAM STRUCTURE.....	44
Input File.....	44
Geometric, Numerical and Material Input.....	44
Loading Input.....	48
Program Flow Chart.....	48
Output File.....	51
CHAPTER 8	
EXAMPLES.....	54
Bending Examples.....	54
Free Expansion Case.....	56
Contact Examples.....	56
CHAPTER 9	
CONCLUSIONS.....	67
APPENDIX A.....	68
APPENDIX B.....	73
REFERENCES.....	75

LIST OF FIGURES

Figure 1.1 Representative hydroformed components and assemblies.....	2
Figure 1.2 Principal hydroforming tooling diagram.....	2
Figure 2.1 Shell element at original time t_0 and current time t (Total Lagrangian).....	10
Figure 2.2 Shell mid-surface at reference time 0t and current time t (Total Lagrangian).....	10
Figure 3.1 A rectangular tube and the assumed global coordinate system.....	14
Figure 3.2 Geometry of a straight segment.....	18
Figure 3.3 Geometry of a circular segment.....	18
Figure 5.1 Contact tolerance.....	25
Figure 5.2(a) The computational mesh (b) The normal vector and tangent vector.....	26
Figure 5.3 The associated die segment with contact node.....	28
Figure 5.4 The projection algorithm.....	30
Figure 5.5 Coulomb friction model.....	32
Figure 6.1 A schematic of tool-workpiece check.....	40
Figure 6.2 Flow chart for contact iteration.....	42
Figure 7.1 Flow chart of the program.....	49
Figure 8.1 Stretching/bending of a rectangular section.....	57
Figure 8.2 Stretching/bending of a circular section.....	57
Figure 8.3 Bending a tube to collapse.....	58
Figure 8.4 Strain and displacement result compared with ABAQUS.....	59

Figure 8.5a A round aluminum tube was expanded into a square die with sharp-corners.....	60
Figure 8.5b Final shape from ABAQUS.....	60
Figure 8.6a Hoop strain distribution compared with experiment.....	61
Figure 8.6b Intermediate shapes of the tube during hydroforming.....	62
Figure 8.7a Circumferential strain distribution after bending.....	63
Figure 8.7a Circumferential strain distribution after bending.....	64

INTRODUCTION

Hydroforming offers a way to cut material and manufacturing costs while improving product performance in a variety of applications. Advantages include material savings, making shapes that cannot be made by conventional manufacturing methods, and the ability to shape dissimilar tailor-welded materials. It reduces tooling, part, and labor costs, while significantly improving product performance (Anon, 1997).

The process currently is either being used or being considered for making a wide range of complex cylindrical, flat and tubular components. Cylindrical parts include gas cylinders, washing-machine drums, and cooker cavities. Flat components include auto body panels, fuel tanks, and aerospace parts.

Tube hydroforming is receiving the greatest attention, especially in the auto industry (Vari-Form Inc, 1998), because existing multi-piece, stamped/welded assemblies in auto body and frame structures potentially can be replaced with less expensive hydroformed parts that are lighter, stronger and more precise (Figure 1.1).

In tube hydroforming, internal pressure is applied to form a tubular metal blank into a structural component having a closed cross section. As shown in Figure 1.2, a straight or prebent tube is placed in an open die, the die is closed, the tube ends are sealed, and the tube is filled with a hydraulic fluid. Internal hydraulic pressure forces the tube to conform to the shape of the die cavities, producing a part having different cross-section shapes.

S
Bot



Figure 1.1 --- Representative hydroformed components and assemblies
 From left to right: instrument panel support beam, engine-cradle assembly.
 Photo courtesy Vari-Form, Woodstock, Ontario, Canada.

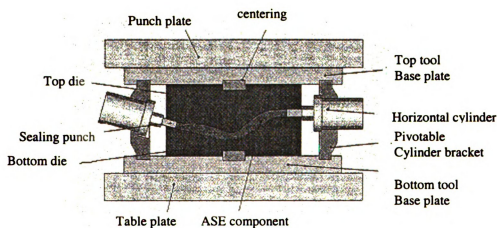


Figure 1.2 --- Principal hydroforming tooling diagram
 Courtesy Schafer Hydroforming, Wilnsdorf, Germany.

The thesis presents a "cross-section" analysis method for calculating tube stretching and bending followed by hydroforming and expansion to fill the die in the hydroforming process.

The present method employs a number of simplifying assumptions. The principal geometrical assumption is that the cross-section of the extrusion can be of any shape consisting of straight-line segments and circular arcs. All segments making up the cross-section are assumed to be relatively thin and of constant thickness. The deformation of the member is assumed not to vary along the length. Hence, the analysis can be considered to be a "section" analysis.

The material is assumed to be elastic-plastic and to satisfy the plasticity model that takes into account rate-independent, work hardening and normal anisotropy (Pourboghraat et al, 2000).

At the tool-tube interface, the frictional stress is assumed, on the basis of ordinary Coulomb friction, to be proportional to the contact pressure whenever relative sliding occurs.

By using the virtual work principle and constitutive equation, the equilibrium equation can be derived. Numerical solution obtained from a Total-Lagrangian formulation of a general shell theory is employed. The boundary friction condition is introduced into the formulation in the form of penalty function, which imposes the constraints directly into the tangent stiffness matrix. The Newton-Raphson algorithm is used to solve the nonlinear equation.

1.

qu

ap

hy

m

hy

kn

an

en

pro

alter

desig

CHAPTER 1

LITERATURE REVIEWS

1.1 Hydroforming Concept

Hydroforming has been one of the fundamental sheet metal forming processes for quite a long time, having been developed at least since pre-World War II, when it was applied to the German aircraft industry (Zhang, 1997). About 30 years ago, the first hydroformed parts were fabricated by expanding a straight or prebent tube to make manifold elements and components of similar geometry for sanitary use. Today, many hydroformed parts are already in mass-production in the automotive industry. Well-known hydroformed automotive applications include exhaust manifolds, exhaust pipes and subframes, such as radiator enclosures, space frames, dash assemblies, frame rail, engine cradles, etc.(Dohman et al, 1997)

According to its features, hydroforming can be classified as the following processes (Zhang, 1999 and Siegert et al, 2000):

1. Flat sheet hydroforming or hydroforming deep drawing
2. Tube hydroforming or hydrobulging of tubular components
3. Hydromechanical deep drawing process
4. New variation of hydroforming including the integral hydrobulge forming (IHBF) of sheet shell products and viscous pressure forming (VPF) processes

In this thesis, we focus on tube hydroforming that has become an economic alternative to various stamping processes with the availability of advanced machine design and controls.

1

s

h

a

k

to

fe

(1

Tube hydroforming offers several advantages as compared to conventional manufacturing via stamping and welding (Ahmetoglu et al, 2000). These include:

- (a) part consolidation (stamped and resistance welded two or more pieces of a box section can be manufactured in one operation from a hollow component)
- (b) weight reduction through more efficient section design and tailoring of the wall thickness
- (c) improved structural strength and stiffness
- (d) lower tooling cost due to fewer parts
- (e) fewer secondary operation (no welding of sections required and holes may be punched during hydroforming)
- (f) tight dimensional tolerances and low springback
- (g) reduced scrap

While numerous variations of hydroforming exist, the basic principle remains the same: utilize fluid pressure to form a component. Both traditional high-pressure hydroforming and pressure sequence hydroforming are presented in Longhouse (1998) and Morphy (1997).

If hydroforming technology is to be applied economically, it is essential to have knowledge of the avoidance of failure cases as well as of the behavior of the tube in the tool under the compressive stress and forces that are exerted by the machine (i.e., axial feed). Several failure modes, buckling, wrinkling and bursting are shown in Dohmann (1996).

dra

ele

ass

inc

arb

exa

wa

me

thi

co

an

ph

of

of

de

for

(19

wh

for

1.2 Numerical Simulation

Kobayashi (1989) has worked on several sheet forming problems including drawing, bulging, stretch forming and bending, solving the problems using a finite element method based on incremental strain theory. In his work, the material was assumed as rigid-plastic and anisotropy and work hardening characteristics were included. An elastic-plastic FEM formulation of stretch forming for a punch and a die of arbitrary shape was introduced by Wang and Bundiansky (1978), which is a classic example verified by ABAQUS. A rigid-viscoplastic material model FEM formulation was presented by Germain, Chung and Wagoner (1989).

All the numerical analyses mentioned above were obtained using simple membrane theory which does not include the variation of stresses through the sheet thickness. This approximation is justified when the thickness of sheet material is small compared to the curvature of the sheet surface, the radius of either the punch or the die, and when in-plane stretch dominates bending. However, in order to simulate bending phenomena such as the early deformation in stretch forming, spring-back etc., inclusion of the bending stress is necessary. A total Lagrangian formulation based on an extension of a thin shell theory which takes into account large membrane and bending strain was derived by Wang and Tang (1988). An updated Lagrangian and plane-strain bending formulation based on nonlinear thin-shell theory was employed by Choudhry and Lee (1994). A general purpose finite element program for analysis of forming processes, which was implemented in MARC, was introduced by Nagtegaal and Rebelo (1988).

Built on the successful application of finite element method on sheet metal forming, explicit finite element method is being applied to hydroforming of tubular parts

by Ni (1994), bulging process by Hu et al. (1997), and a sheet metal operation involving punch stretching, drawing and hydroforming by Hsu and Chu (1995). In Noh and Yang (1998) work, a general formulation for hydroforming of arbitrarily shaped boxes was expressed.

1.3 Friction and Contact Problem

Friction and contact between sheet and die play an important role in hydroforming processes. Classical Coulomb's law is capable of describing only friction effects between effectively rigid bodies and gross sliding of one body relative to another, However if Coulomb's law is applied pointwise in contact problem, then the contact stress developed normal to the contact surface is ill defined. In Oden and Pires (1983), nonlocal and nonlinear friction laws and variational principles for contact problems were introduced.

A method of discretizing the die boundary condition considered for the analysis of metal forming processes with arbitrary shaped dies was employed by Oh (1982).

T

c

th

th

D

a

an

2.

$t(=$

be

the

wh

the

In E

Eq.

CHAPTER 2

THIN SHELL THEORY

The deformation of the mid-surface of an element in the plane containing the meridian curve will be considered. The deformation of the element will be obtained from the theory of thin shells and Figure 2.1-2.2 show the mid-surface of an element of the sheet at the initial time t_0 , reference time 0t and at the current time t as it bends and stretches. Derivation of principal curvatures, stretches of a shell element undergoing an axisymmetric deformation was discussed in (Pourboghraat, F. et al, 2000) using both total and updated Lagrangian formulations. These formulations are used in the program.

2.1 Principal Stretch (Total Lagrangian Formulation)

Figure 2.1 shows a flat element at the initial time t_0 and at the current time $t(={}^0t+\Delta t)$ as it bends and stretches. By referring to Figure 2.1, the following relationship between the current and the initial position vectors and the total displacement vector for the mid-surface of the element can be written:

$$\underline{x} = \underline{X} + \underline{U} \quad (2.1)$$

where the initial position vector \underline{X} and the total displacement vector \underline{U} are, defined in the global coordinate system,

$$\underline{X} = \begin{bmatrix} X_1 \\ 0 \end{bmatrix}, \quad \underline{U} = \begin{bmatrix} u \\ w \end{bmatrix} \quad (2.2)$$

In Eq.(2.2), u and w are the total displacements of the mid-surface. By substituting from Eq.(2.2) into (2.1), the position vector \underline{x} becomes

$$\underline{x} = \begin{bmatrix} X_1 + u \\ w \end{bmatrix} \quad (2.3)$$

To calculate the principal stretch in the radial direction, we will consider the unit tangent vector, $\hat{\underline{a}}$, of the current mid-surface, i.e.

$$\hat{\underline{a}} = \frac{d\underline{x}}{ds} = \frac{d\underline{x}}{dS} \frac{dS}{ds} = \frac{d\underline{x}}{dX_1} \frac{1}{\lambda_1^0} = \begin{bmatrix} 1 + u_{,X_1} \\ w_{,X_1} \end{bmatrix} \frac{1}{\lambda_1^0} \quad (2.4)$$

where $\lambda_1^0 = ds/dS$. Here, s and S are travel length of the current and initial surfaces from center, respectively, and the comma stands for the differentiation with respect to X_1 .

Then, by calculating the magnitude of vector $\hat{\underline{a}}$ from Eq.(2.4) and setting it equal to unity, λ_1^0 can be calculated to be:

$$\|\hat{\underline{a}}\| = \sqrt{\hat{\underline{a}} \cdot \hat{\underline{a}}} = 1.0 \quad (2.5)$$

$$\lambda_1^0 = [(1 + u_{,X_1})^2 + w_{,X_1}^2]^{\frac{1}{2}} \quad (2.6)$$

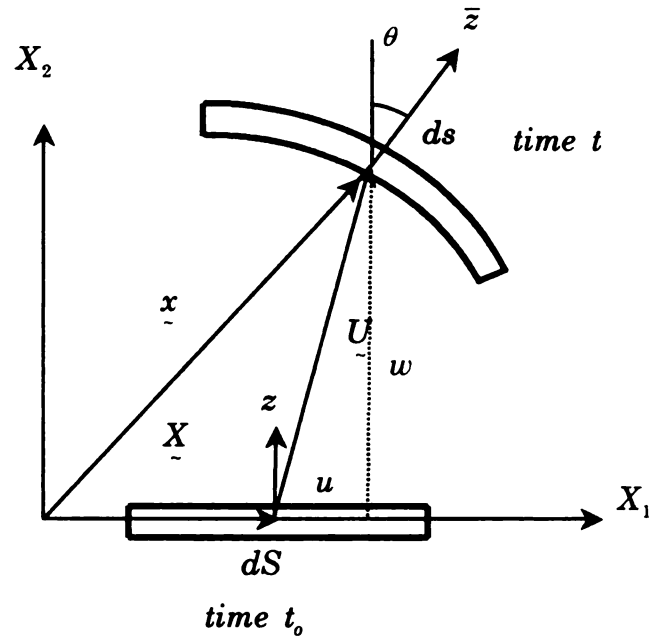


Figure 2.1 Shell element at original time t_0 and current time t (Total Lagrangian)

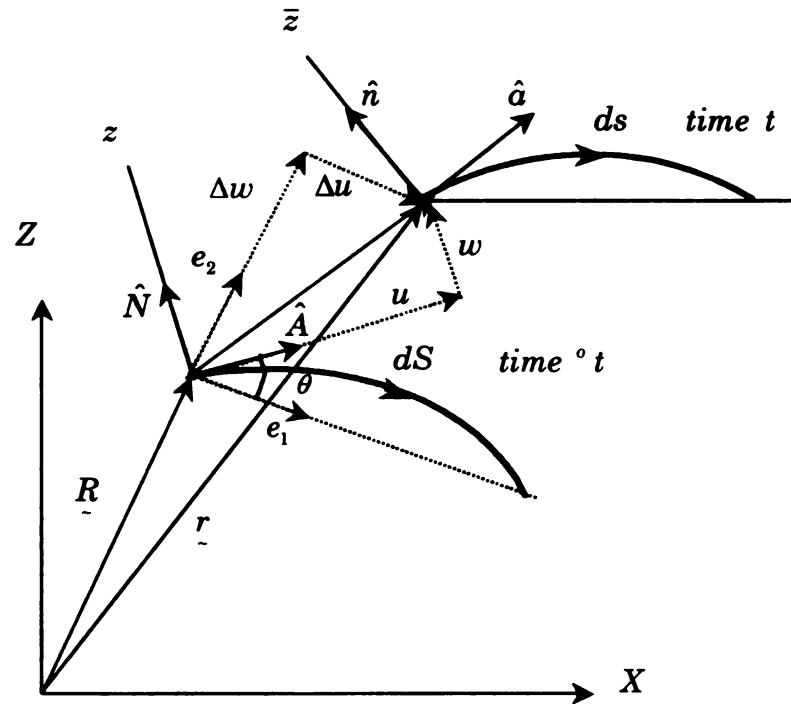


Figure 2.2 Shell mid-surface at reference time ${}^\circ t$ and current time t (Updated Lagrangian)

2.2 Principal Curvature and Stretch (Updated Lagrangian)

After bending and stretching, the principal mid-surface curvature, k_1 , of a shell element at the current configuration, $t(={}^0t+\Delta t)$, can be calculated from the known information about the element at the reference configuration (time 0t , see Figure 2.2), as follows:

$$\underline{r} = \underline{R} + u \underline{\hat{A}} + w \underline{\hat{N}} \quad (2.7)$$

where \underline{R} is the reference configuration at time ${}^0\tau$ and u and w are incremental displacements defined in Figure 2.2. In Eq.(2.7), the unit tangent vector $\underline{\hat{A}}$ and the unit principal normal vector $\underline{\hat{N}}$ to the mid-surface of the reference are defined as

$$\underline{\hat{A}} = \frac{\partial \underline{R}}{\partial S} = \underline{R}_{,s} \quad (2.8)$$

$$\underline{\hat{N}} = \frac{\underline{\hat{A}}_{,s}}{K_1} \quad (2.9)$$

where K_1 is the curvature. Therefore,

$$\underline{\hat{N}} \cdot \underline{\hat{A}} = 0 \quad (2.10)$$

and

$$-K_1 \underline{\hat{A}} = \underline{\hat{N}}_{,s} \quad (2.11)$$

To calculate the current curvature, k_1 , the unit tangent vector $\hat{\underline{a}} = \frac{\underline{a}}{\|\underline{a}\|}$ and the

unit principal normal vector of the mid-surface of the shell $\hat{\underline{n}} = \frac{\underline{n}}{\|\underline{n}\|}$ are calculated.

Using Eq.(2.7), the tangent vector \underline{a} is found as:

$$\underline{a} = \frac{\partial \underline{r}}{\partial S} = \underline{r}_{,s} = \underline{R}_{,s} + u_{,s} \hat{\underline{A}} + u \hat{\underline{A}}_{,s} + w_{,s} \hat{\underline{N}} + w \hat{\underline{N}}_{,s} \quad (2.12)$$

By substituting from Eqs.(2.8), (2.9) and (2.11) into (2.12), and re-arranging, the following expression results:

$$\underline{a} = \frac{\partial \underline{r}}{\partial S} = \underline{r}_{,s} = (1 + u_{,s} - K_1 w) \hat{\underline{A}} + (w_{,s} + K_1 u) \hat{\underline{N}} = c \hat{\underline{A}} + d \hat{\underline{N}} \quad (2.13)$$

The principal incremental stretch of the mid-surface in the radial direction calculated from the magnitude of the base vector \underline{a} in Eq.(2.13) is

$$\lambda_1 = \|\underline{a}\| = \sqrt{\underline{a} \cdot \underline{a}} = \sqrt{c^2 + d^2} = [(1 + u_{,s} - K_1 w)^2 + (w_{,s} + K_1 u)^2]^{\frac{1}{2}} \quad (2.14)$$

The current length of the mid-surface of the shell in the radial direction, ds , is calculated from the reference length, dS , and λ_1 as follows:

$$ds = \lambda_1 dS \quad (2.15)$$

The unit principal normal vector of the surface of the current shell, $\hat{\underline{n}}$, is

$$\hat{\underline{n}} = \frac{-d \hat{\underline{A}} + c \hat{\underline{N}}}{\lambda_1} \quad (2.16)$$

which, from Eqs.(2.13), (2.14) and (2.16), shows that $\hat{n} \cdot \hat{a} = 0$. The current principal curvature of the shell, k_1 , can now be found as:

$$k_1 = -\hat{a} \cdot \hat{n}_{,s} = -\underline{r}_{,s} \cdot \hat{n}_{,s} = -\frac{1}{\lambda_1^2} \underline{a} \cdot \hat{n}_{,s} \quad (2.17)$$

where \underline{a} is given by Eq.(2.12) and $\hat{n}_{,s}$ can be derived from Eq.(2.16):

$$\hat{n}_{,s} = \frac{d\hat{n}}{dS} = \frac{\lambda_1 \cdot (d_{,s} \hat{A} + c_{,s} \hat{N} - K_1 c \hat{A} - K_1 d \hat{N}) - \lambda_{1,s} \cdot (-d \hat{A} + c \hat{N})}{\lambda_1^2} \quad (2.18)$$

In Eq.(2.18), $\lambda_{1,s}$ is assumed to vanish within an element and the above expression simplifies as :

$$\hat{n}_{,s} = -\frac{(d_{,s} + K_1 c) \hat{A} + (-c_{,s} + K_1 d) \hat{N}}{\lambda_1} \quad (2.19)$$

By substituting from Eqs.(2.13), (2.14) and (2.19) into Eq.(2.17), the current centerline curvature of the shell, k_1 , can be found:

$$k_1 = \frac{cd_{,s} - dc_{,s} + K_1 \lambda_1^2}{\lambda_1^3} \quad (2.20)$$

It should be noted that it is possible to recover Eq.(2.6), for total Lagrangian formulation, From Eq.(2.14). This is done by setting the reference curvature K_1 equal to zero for a flat sheet, replacing S with X_1 and treating the incremental displacement u and w as total displacements in Eqs.(2.13) and (2.14). Similarly, the current curvature of the shell, k_1 , can be calculated from the initial configuration by setting K_1 equal to zero, replacing λ_1 with λ_1^o and S with X_1 and treating u and w as total displacements in Eq.(2.20)

$$k_1 = \frac{[-w_{,x_1} u_{,x_1 x_1} + (1 + u_{,x_1}) w_{,x_1 x_1}]}{(\lambda_1^o)^3} \quad (2.21)$$

CHAPTER 3

KINEMATICS

Based on the general thin shell formulations in Chapter 2, the formulations for finite strain and small rotation have been derived for the straight line segment and arc segment that are used in the program. (Derivation in details can be seen in Appendix A).

The formulation in Corona and Pourboghra (1998) focuses on a closed structural member, such as a thin-walled hollow tube, that is subjected to combined tension and bending loadings. The cross-section of the tube can be of any closed or open shape consisting of straight-line segments and circular arcs (see Figure 3.1).

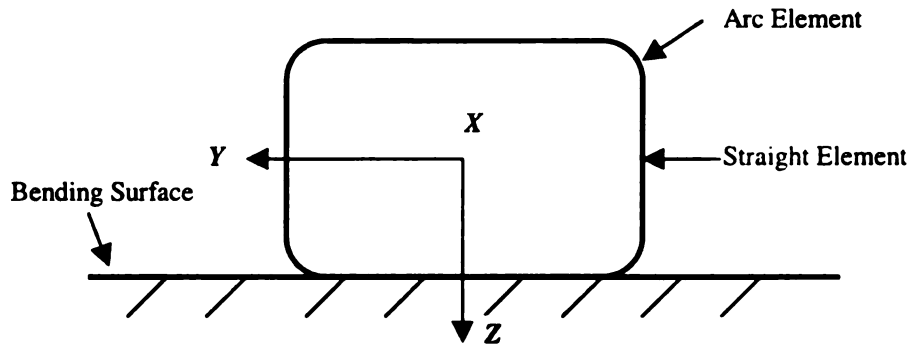


Figure 3.1. A rectangular tube and the assumed global coordinate system.

For the purpose of modeling, all segments making up the cross-section are assumed to be thin and of constant thickness. The length of the straight segments should be greater than ten times the thickness, while the radius of the circular arcs should be greater than eight times the thickness. The deformation of the structural member is

assumed not to vary along its length (in X-direction). Hence, the analysis can be done for a section along the axial dimension, as shown in Figure 3.1.

3.1 Straight Segment

The rectangular cross-section shown in Figure 3.1 lies in the plane defined by the Y and Z -axes, while the X -axis is in the axial (length) direction of the member. This figure indicates that the curvature κ_z of a tube bent about the Y -axis will match that of the bending surface. A simultaneous bending about the Z -axis is also possible in order to impart an additional curvature κ_y to the tube. In this formulation, the initial geometry of the cross-section is specified by first defining the Y - Z coordinates of a set of nodes and then defining the segments. Two nodes must bind each segment.

For the straight segment in Figure 3.2, the local coordinates of the segment are s along the segment and z in the through-thickness direction. The initial segment geometry is defined by the location of the point $s = 0$ given by Y_0 and Z_0 , the orientation angle θ , the length l_0 and the thickness t of the segment. The position $z=0$ is located at the mid-surface of the segment, indicated by the dashed line. The displacement components of the mid-surface are u and w along the original s and z directions respectively. The rotation of a line is given by β

$$\beta = -\frac{dw}{ds} = -w_{,s} \quad (3.1)$$

The axial strain component of a point is given by:

$$\varepsilon_x = \varepsilon_x^0 + \kappa_z \xi - \kappa_y \eta \quad (3.2)$$

where ε_x^0 is the axial strain (axial feed) along the length of the tube (X -direction) and

$$\xi = Z_0 + (s + u) \sin \theta - w \cos \theta + z(-\cos \theta + \beta \sin \theta) \quad (3.3a)$$

$$\eta = Y_0 + (s + u) \cos \theta + w \sin \theta + z(\sin \theta + \beta \cos \theta) \quad (3.3b)$$

The strain component ϵ_s along s is given by

$$\epsilon_s = \epsilon_s^0 + \kappa_s z \quad (3.4)$$

where ϵ_s^0 is the membrane strain component given by

$$\epsilon_s^0 = u_{,s} + \frac{1}{2} u_{,s}^2 + \frac{1}{2} w_{,s}^2 \quad (3.5)$$

where the local curvature is given by

$$\kappa_s = \frac{w_{,ss}}{(1 + w_{,s}^2)^{\frac{3}{2}}} \quad (3.6)$$

3.2 Circular Arc Segments

For the circular arc segment shown in Figure 3.3, the local coordinates of the segment are the angle ϕ and the through-thickness z . The initial geometry of the segment is specified by 1) the coordinates of the center of the arc, Y_c and Z_c , 2) the angle ϕ_0 , which locates the line where $\phi = 0$, 3) the radius R , 4) the angle spanned by the arc $\Delta\phi$, 5) and the thickness of the segment t . As in the straight segment, the mid-surface is the origin for z and is indicated by the dashed line. The rotation of a line, β , can be given as

$$\beta = \frac{u - \frac{dw}{d\phi}}{R} = \frac{u - w_{,\phi}}{R} \quad (3.7)$$

The axial strain of a point is given by Eq.(3.2), but for an arc

$$\xi = Z_c + (R + w) \sin \bar{\phi} + u \cos \bar{\phi} + z(\sin \bar{\phi} + \beta \cos \bar{\phi}) \quad (3.8a)$$

$$\eta = Y_c + (R + w) \cos \bar{\phi} - u \sin \bar{\phi} + z(\cos \bar{\phi} - \beta \sin \bar{\phi}) \quad (3.8b)$$

where $\bar{\phi} = \phi_0 + \phi$. The tangential strain is given by

$$\varepsilon_\phi = \varepsilon_\phi^0 + \kappa_\phi z \quad (3.9)$$

where

$$\varepsilon_\phi^0 = \left(\frac{u_{,\phi} + w}{R} \right) + \frac{1}{2} \left(\frac{u - w_{,\phi}}{R} \right)^2 + \frac{1}{2} \left(\frac{w + u_{,\phi}}{R} \right)^2 \quad (3.10)$$

and

$$\kappa_\phi = \frac{cd_{,\phi} - dc_{,\phi} + \lambda_1^2/R}{\lambda_1^3} \quad (3.11)$$

where $c = 1 + \frac{1}{R}(u_{,\phi} - w)$, $d = \frac{1}{R}(w_{,\phi} + u)$ and $\lambda_1 = \sqrt{c^2 + d^2}$

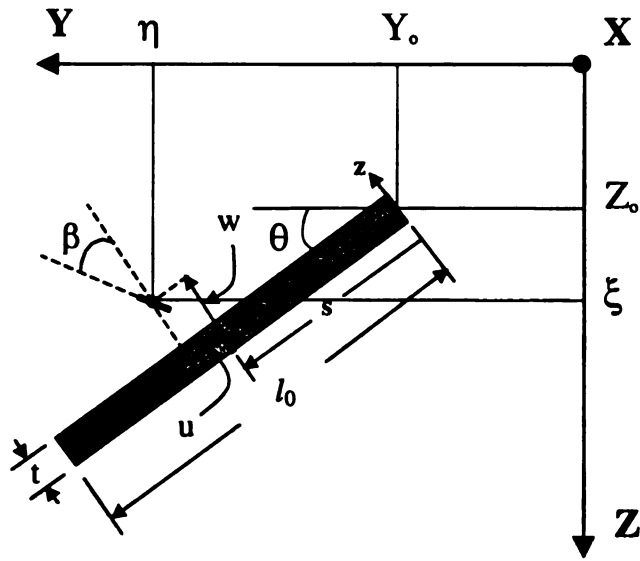


Figure3.2 Geometry of a straight segment

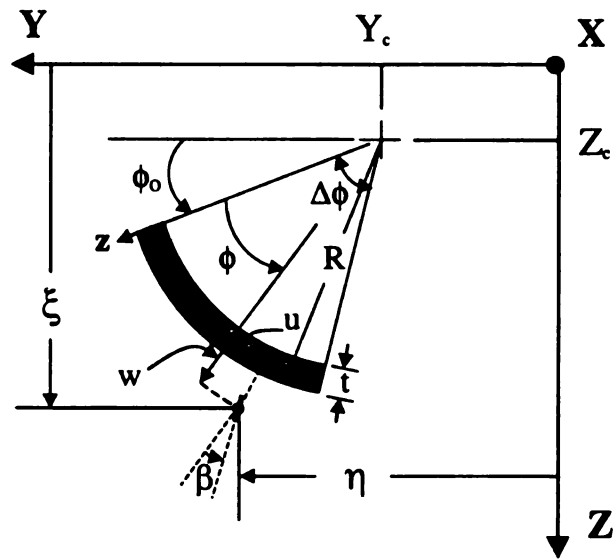


Figure3.3 Geometry of a circular arc segment

3.3 Constraints

Since the cross-section is made of several independent segments which have their own local coordinate systems and variables, it is necessary to enforce compatibility of deformations at junction of two or more segments. Two constraint equations are used to ensure compatibility of displacements and one to ensure compatibility of rotation between two segments. Therefore, at a junction where M segments come together, $3(M-1)$ constraint equations need to be enforced. At a junction between two straight segments having orientation angle θ_1 and θ_2 and components u_1, w_1 and u_2, w_2 , the two displacement compatibility conditions can be written in terms of the displacement components in the Y and Z directions as follows:

$$u_2 \cos \theta_2 + w_2 \sin \theta_2 - u_1 \cos \theta_1 - w_1 \sin \theta_1 = 0 \quad (3.12)$$

$$u_2 \sin \theta_2 - w_2 \cos \theta_2 - u_1 \sin \theta_1 + w_1 \cos \theta_1 = 0 \quad (3.13)$$

The rotation constraint requires that the angle between segments at a junction remain unchanged. For the current example, if the rotations of the two members at the junction are β_1 and β_2 , compatibility condition is

$$\beta_2 - \beta_1 = 0 \quad (3.14)$$

CHAPTER 4

CONSTITUTIVE EQUATION

The elastic-plastic model which has been implemented in the program has been developed by Pourboghra et al (2000). It is based on the isotropic hardening model. The uniaxial stress-plastic strain curve of the material is given by

$$\bar{\sigma} = K(\bar{\epsilon} + \bar{\epsilon}_0)^N \quad (4.1)$$

where $\bar{\sigma}$ is the effective stress and $\bar{\epsilon}$ is the plastic strain. Parameters K , N and $\bar{\epsilon}_0$ are material constants. The elastic strain increment is related to the stress increment through the equations of linear, isotropic elasticity with Young's modulus E and Poisson's ratio. The yield function allows for anisotropic yielding of the material. The yield function is given by

$$f = \frac{\sigma_x^2 + \sigma_s^2 + R(\sigma_x - \sigma_s)^2}{1 + R} - \sigma_y^2 = 0 \quad (4.2)$$

where σ_y is the yield stress and R is an anisotropy parameter.

During loading, Hooke's law is used to calculate stress below the elastic limit; i.e., $\bar{\sigma} \leq \sigma_y$, where σ_y is the initial yield stress of the sheet obtained from a uniaxial tensile test. Beyond the elastic limit; i.e., $\bar{\sigma} > \sigma_y$, the co-rotational time derivative of stress (Jaumann stress rate) is calculated, for a given strain rate, from an elasto-plastic constitutive equation (Becker, 1992):

$$\dot{\bar{\sigma}} = \left[\bar{L} - \frac{\bar{L} : \bar{P} \bar{P} : \bar{L}}{\bar{P} : \bar{\sigma} + h \frac{\bar{P} : \bar{L} : \bar{P}}{\bar{\sigma}}} \right] : \bar{D} \quad (4.3)$$

Here $\dot{\underline{\sigma}}$ and $\underline{D}(= \underline{D}^e + \underline{D}^p)$ are the Jaumann rate of stress and strain rate tensors, respectively, $\underline{\sigma}$ is the stress tensor, $\bar{\sigma}$ is the material flow strength, $h(= \partial \bar{\sigma} / \partial \bar{\epsilon})$ is the plastic hardening parameter, \underline{L} is the fourth order elastic tensor and $\underline{P}(= \partial \phi / \partial \underline{\sigma} / \|\partial \phi / \partial \underline{\sigma}\|)$, where $\|\partial \phi / \partial \underline{\sigma}\| = \sqrt{\partial \phi / \partial \underline{\sigma} : \partial \phi / \partial \underline{\sigma}}$, is the second order tensor representing the unit normal to the flow potential surface. The plastic strain rate, associated with Eq.(4.3), is calculated from the following expression:

$$\dot{\bar{\epsilon}} = \frac{\underline{P} : \underline{L} : \underline{D} - \underline{P} : \dot{\underline{\sigma}}}{\frac{\bar{\sigma}}{\underline{P} : \underline{\sigma} : \underline{L} : \underline{P}}} \quad (4.4)$$

The fourth order elastic tensor $\underline{L}(= L_{ijkl})$ used in this work is the standard tensor for the isotropic elasticity, which has only two independent components.

CHAPTER 5

CONTACT ALGORITHM

The simulation of hydroforming processes requires the ability to model the contact phenomena. The analysis of contact behavior is complex because of the requirement to accurately track the motion of multiple geometric bodies, and the motion due to the interaction of these bodies after the contact. The numerical objective is to detect the motion of the bodies, apply a constraint to avoid penetration, and apply appropriate boundary condition to simulate the frictional behavior (Marc's Theory and user information).

5.1 Numerical Procedures for Contact

Two widely used procedures are available, namely the Lagrange multiplier method and penalty method, which will be introduced here briefly. Both, the Lagrange multiplier method and penalty method operate on variational formulation of problem under consideration (Bathe, 1982).

For purpose of demonstration, consider the total potential energy Π_p of a discrete system for steady-state analysis,

$$\Pi_p = \frac{1}{2} \mathbf{U}^T \mathbf{K} \mathbf{U} - \mathbf{U}^T \mathbf{R} \quad (5.1)$$

The constraint equations can be expressed as

$$\mathbf{C} \mathbf{U} = 0 \quad (5.2)$$

In the Lagrange multiplier method we amend the r.h.s. of (5.1) to obtain

$$\Pi_p^* = \frac{1}{2} \mathbf{U}^T \mathbf{K} \mathbf{U} - \mathbf{U}^T \mathbf{R} + \lambda^T \mathbf{C} \mathbf{U} \quad (5.3)$$

where λ contains as many Lagrange multipliers as there are constraint equations, and invoke that $\delta \Pi_p^* = 0$, which gives

$$\begin{bmatrix} \mathbf{K} & \mathbf{C}^T \\ \mathbf{C} & \mathbf{0} \end{bmatrix} \begin{Bmatrix} \mathbf{U} \\ \lambda \end{Bmatrix} = \begin{Bmatrix} \mathbf{R} \\ \mathbf{0} \end{Bmatrix} \quad (5.4)$$

The second of Eq.(5.4) is Eq.(5.2), the equation of constraint. Eq.(5.4) are solved for both \mathbf{U} and λ . The λ_i may be interpreted as force of constraint.

In the penalty method we also amend the r.h.s. of (5.1) but without introducing an additional variable. Now we use

$$\Pi_p^* = \frac{1}{2} \mathbf{U}^T \mathbf{K} \mathbf{U} - \mathbf{U}^T \mathbf{R} + \frac{1}{2} \mathbf{t}^T \boldsymbol{\alpha} \mathbf{t} \quad (5.5)$$

in which $\mathbf{t} = \mathbf{C} \mathbf{U}$, and $\mathbf{t} = \mathbf{0}$ implies satisfaction of the constraint. The usual potential Π_p of the system can be augmented by a penalty function $\frac{1}{2} \mathbf{t}^T \boldsymbol{\alpha} \mathbf{t}$, where $\boldsymbol{\alpha}$ is a diagonal matrix of penalty numbers α_i . The condition $\delta \Pi_p^* = 0$ now yields

$$[\mathbf{K} + \mathbf{C}^T \boldsymbol{\alpha} \mathbf{C}] \mathbf{U} = \mathbf{R} \quad (5.6)$$

If $\boldsymbol{\alpha} = \mathbf{0}$, the constraints are ignored. As $\boldsymbol{\alpha}$ grows, \mathbf{U} changes in such a way that the constraint equations are more nearly satisfied.

It is difficult to assess which method, the Lagrange multiplier method and penalty method, is better in the finite element implementation. However, it can be mentioned that the Lagrange multiplier method introduces a large number of independent variables. Also, the diagonal terms of the stiffness matrix corresponding to the λ always become zero and special attention is required during the assembly of the stiffness matrix so that an equation corresponding to any λ does not become the first one in the stiffness

equations after applying the boundary conditions (Kobayashi et al, 1989). In comparison with Lagrange multiplier, penalty functions have the advantages of introducing no new variables and requiring no special care for the order of unknowns for successful equation solving. Their implementation can be as easy as assigning a high modulus for an element already in the program. Thus, we use penalty functions to implement the constraints in contact problem.

Effectively, the penalty procedure constrains the motion by applying a penalty to the amount of penetration that occurs in the hydroforming processes. The penalty approach can be considered as analogous to a nonlinear spring between the two bodies. Using the penalty approach, some penetration occurs with the amount being determined by the penalty constant or function. The choice of the penalty value can also have a detrimental effect on the numerical stability of the global solution procedure.

5.2 Detection of Contact

During the contact process, each potential contact node is first checked to see whether it is near a contact segment. The contact segments are either edges of the other 2D deformable bodies, faces of 3D deformable bodies, or segments from rigid bodies that stand for the dies in tube hydroforming process. The motion of the nodes is checked to see whether it has penetrated a surface by determining whether it has crossed a segment. The determination of when contact occurs and the calculation of the normal vector are critical to the numerical simulation. In this part, the normal vector of potential contact node has been pre-defined and a so-called cross-product algorithm is used to determine which segment is associated with the potential contact node.

5.2.1 Contact Tolerance

During the contact process, it is unlikely that a node exactly contact the surface. For this reason, a contact tolerance is associated with each surface (Figure 5.1). If a node is within the contact tolerance, it is considered to be in contact with the segment. The contact tolerance is calculated by the program as 5% of the thickness of segment.

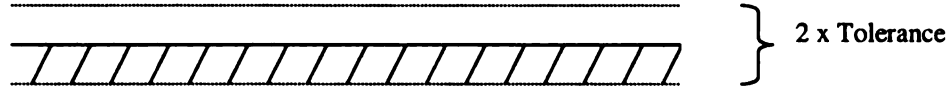


Figure 5.1 Contact tolerance

5.2.2 Normal Vector and Tangential Vector

In order to track the motion of each potential contact node, it is important to define the normal vector and tangential vector of the node (Sheet-S).

The normal and tangential vectors of the nodes of the mesh (Figure 5.2(a)) can be calculated as follows: The element i has nodes i and k and length L_i , The element j has nodes k and j and length L_j . The unit normal vector, \mathbf{n} , at the contact node k , as shown in Figure 5.2(b), is evaluated by averaging the normals of elements i and j , \mathbf{N}_i and \mathbf{N}_j , as follows:

$$\mathbf{n} = \frac{\mathbf{N}_i + \mathbf{N}_j}{\|\mathbf{N}_i + \mathbf{N}_j\|} \quad (5.7)$$

By rewriting the normal vector, \mathbf{n} , in the following component form:

$$\mathbf{n} = \frac{1}{ZN} \begin{Bmatrix} Z_x \\ -1 \end{Bmatrix}; \quad ZN = \sqrt{Z_x^2 + 1} \quad (5.8)$$

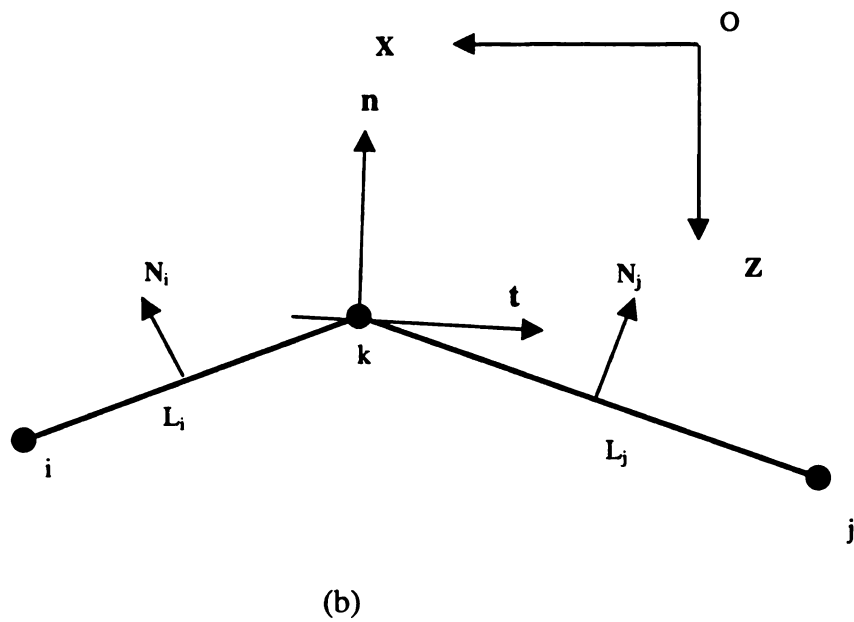
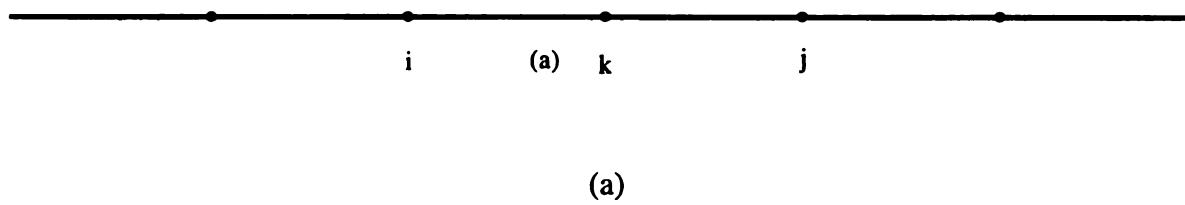


Figure 5.2 (a) The computational mesh and
(b) The normal vector and tangent vector

where Z_x which is interpreted as the slope at node k, can be obtained from Eq.(5.7), in terms of the coordinates, (x,z), of the nodes i, k and j, as follows:

$$Z_x = \frac{L_j(z_k - z_i) + L_i(z_j - z_k)}{L_j(x_k - x_i) + L_i(x_j - x_k)} \quad (5.9)$$

where L_i and L_j are respectively lengths of elements i and j. As seen in Eqs(5.8) and (5.9), the normal vector, \mathbf{n} , at the contact node k, can be expressed in terms of the neighboring nodal coordinates.

The tangent unit vector, \mathbf{t} , at the node k, whose direction is normal to the normal vector, \mathbf{n} , and which is oriented opposite to the sliding direction, is expressed using the orthogonality as follows:

$$\mathbf{t} = \frac{1}{ZN} \begin{Bmatrix} 1 \\ Z_x \end{Bmatrix} \quad (5.10)$$

where ZN and Z_x are defined in Eq.(5.8) and Eq.(5.9), respectively.

Actually, as we can see in Appendix B, when the Fourier series expansion is used to approximate the nodal coordinates, it is easy to exactly define the normal of a node by differentiating the Fourier series without any numerical difficulty.

5.2.3 Condition for Contact Violation

As shown in Figure 5.3, when a node is within the contact tolerance, it is considered to be in contact with the segment. The location of the closest point on the die corresponding to the contact node needs to be determined by using the cross-product algorithm. B_{i-1} , B_i and B_{i+1} are die nodes, A_k is one of the contact nodes and \mathbf{n} is its normal vector.

$$\text{If } (\overrightarrow{A_k B_{i-1}} \times \mathbf{n}) \cdot (\overrightarrow{A_k B_i} \times \mathbf{n}) > 0 \quad (5.11a)$$

$$\text{and } (\overrightarrow{A_k B_i} \times \mathbf{n}) \cdot (\overrightarrow{A_k B_{i+1}} \times \mathbf{n}) < 0 \quad (5.11b)$$

Then, we define segment $B_i B_{i+1}$ to be the segment associated with contact node A_k .

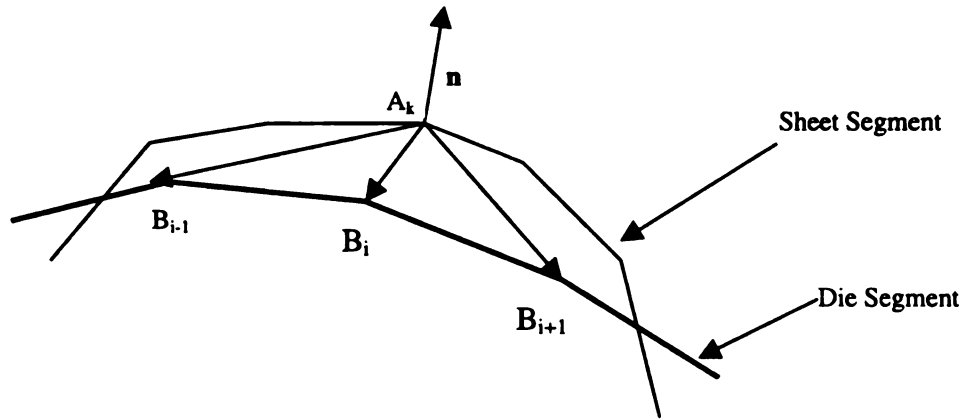


Figure 5.3 The associated die segment with contact node

5.3 The Projection Algorithm

A nodal position produced by the trial solution may penetrate the die. By using the cross-product algorithm, the closest point on the die corresponding to the node can be

found. The nodal coordinates are then modified by a projection scheme such that the node just touches the die surface. There are two ways to bring the penetrated node back to the die surface.

5.3.1 The Iterative Method

The position of a penetrated node is changed to locate it at the tool (die) surface where the normal vector for that node intersects it. After calculating the normal vector, $\mathbf{n} = (n_x, n_z)$, using Eq.(5.8), the tool surface point to be projected $(t \cdot n_x, t \cdot n_z)$ can be iteratively found by solving for the length parameter, t , from the nonlinear equation:

$$S(t \cdot n_x) - t \cdot n_z = 0 \quad (5.12)$$

where $S(x)$ is the tool surface equation.

5.3.2 The Directive Method

As shown in Figure 5.4, PQ is assumed to be the tool segment associated with the penetrated node A, point B is the intersection point between normal vector and PQ, and O is the original point. Based on the following vector equation, the coordinate of point B could be calculated:

$$\overrightarrow{OP} + \overrightarrow{PB} = \overrightarrow{OA} + \overrightarrow{AB} \quad (5.13a)$$

$$\overrightarrow{PB} = \eta_1 \frac{\overrightarrow{PQ}}{\|\overrightarrow{PQ}\|}, \quad \overrightarrow{AB} = -\eta_2 \mathbf{n} \quad (5.13b)$$

where η_1, η_2 are scalar. Once η_1, η_2 are solved from Eq.(5.13), the coordinate of B could be determined.

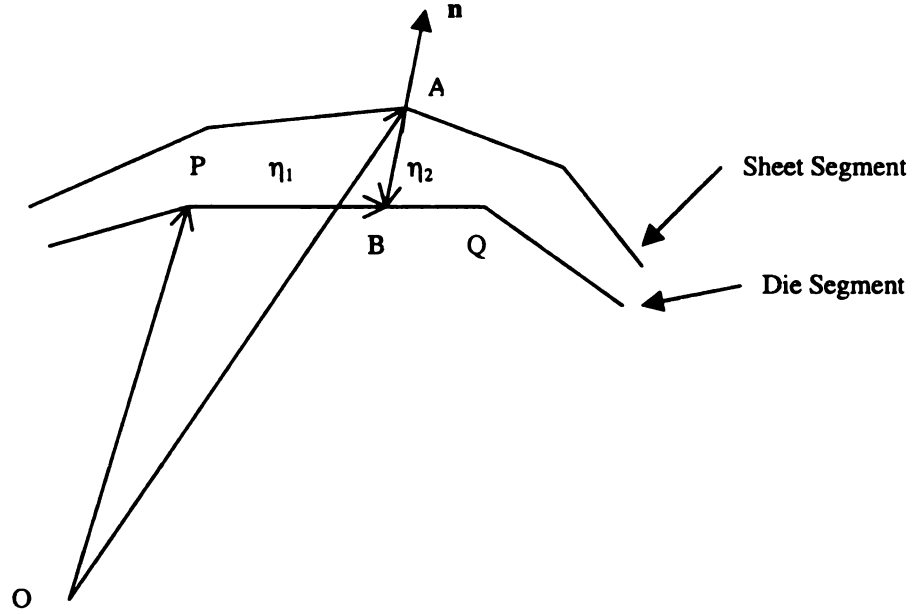


Figure 5.4 The projection Algorithm

5.4 Implementation of Constraint

A node located on the sheet at time $t + \Delta t$, is constrained to move in the tangent direction defined by the trial solution, $\Delta \mathbf{u}^*$. The tangent direction incorporates the Z_x in Eq.(5.9).

The constraint on $\delta \mathbf{u} = (\delta u_x, \delta u_z)$, for contacting nodes is then:

$$\delta \mathbf{u} \cdot \mathbf{n} = 0 \quad (5.14)$$

which by substituting in Eq.(5.8) we will have

$$\delta u_z = Z_x \cdot \delta u_x \quad (5.15)$$

Actually, Eq.(5.15) is the alternative constraint equation, Eq.(5.2), in the contact problem.

5.5 Friction Model

Friction is a complex physical phenomena that involves the characteristics of the surface such as surface roughness, temperature, normal stress, and relative velocity. The numerical modeling of the friction has been simplified to two idealistic models.

The most popular friction model is the Coulomb Friction model. This model is used for most applications. The Coulomb model (Marc's Theory and user information) is:

$$\sigma_{fr} \leq -\mu \sigma_n \cdot \mathbf{t} \quad (5.16)$$

where σ_n is the normal stress

σ_{fr} is the tangential(friction) stress

μ is the friction coefficient

\mathbf{t} is the tangential vector in the direction of the relative velocity

$$\mathbf{t} = \frac{\mathbf{v}_r}{|\mathbf{v}_r|}, \quad \mathbf{v}_r \text{ is the relative sliding velocity.}$$

The Coulomb model is also often written with respect to forces

$$\mathbf{f}_t \leq -\mu \mathbf{f}_n \cdot \mathbf{t} \quad (5.17)$$

where \mathbf{f}_t is the tangential force, \mathbf{f}_n is the normal reaction.

For a given normal stress, the friction stress has a step function behavior based upon the value of \mathbf{v}_r (see Figure 5.5).

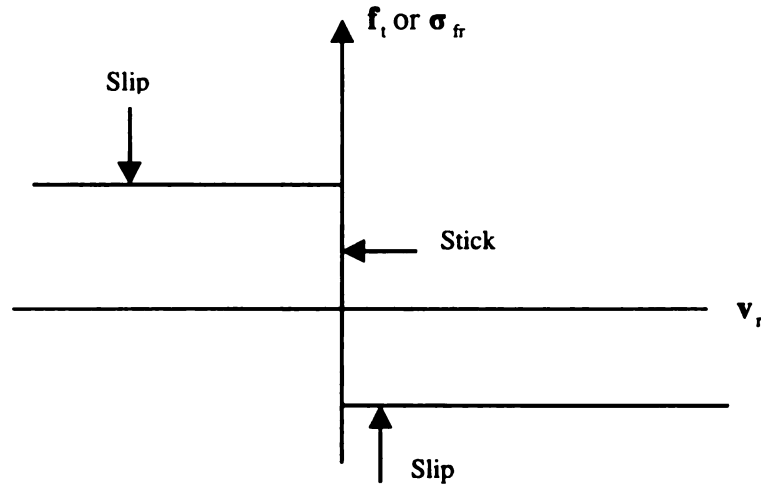


Figure 5.5 Coulomb Friction Model

This discontinuity in the value of σ_{fr} can result in numerical difficulties so a modified Coulomb friction model (Oh, 1982) is implemented:

$$f_s = -mk \frac{\Delta v_s}{|\Delta v_s|} \approx -\frac{2}{\pi} mk \tan^{-1} \left(\frac{\Delta v_s}{u_0} \right) \quad (5.18)$$

where Δv_s is slipping velocity, m is friction factor, k local flow stress in shear and u_0 is very small positive number compared to Δv_s .

When the Coulomb model is used with the stress based model, the integration point stresses are used to calculate the normal stress component of the contact node. The tangential stress is then evaluated and a consistent nodal force is calculated.

5.6 Separation

After a node comes into contact with a surface, it is possible for it to separate in a subsequent iteration or increment. Mathematically, a node should separate when the reaction force between the node and surface becomes tensile or positive.

When contact occurs, a reaction force associated with the node in contact balance the internal stress of the element adjacent to this node. When separation occurs, this reaction force behaves as a residual force (as the force on a free node should be zero). This requires that the internal stresses in the deformable body be redistributed.

CHAPTER 6

NUMERICAL SIMULATION

In this chapter, based on the virtual work principle, the equilibrium equation can be derived. The numerical solution obtained from a Total Lagrangian formulation of a general thin shell theory is employed. In contrast to traditional finite element method, the nodal displacement approximate function based on Fourier series is used. The boundary friction condition is introduced into the formulation in the form of penalty function, which imposes the constraints directly into the tangent stiffness matrix. The Newton-Raphson algorithm is used to solve the nonlinear equilibrium equation.

6.1 Principle of Virtual Work

An equivalent approach to express the equilibrium of the body is to use the principle of virtual work. This principle states that the equilibrium of the body requires that for any compatible, small virtual displacements imposed onto the body, the total internal virtual work is equal to total external virtual work. In the Lagrangian incremental analysis approach we express the equilibrium of the body at time $t + \Delta t$ using the principle of virtual work as:

$$\int_{t+\Delta t_V} {}^{t+\Delta t}\tau_{ij} \delta {}^{t+\Delta t}e_{ij} {}^{t+\Delta t}dV = \int_{t+\Delta t_V} {}^{t+\Delta t}f_i^B \delta u_i {}^{t+\Delta t}dV + \int_{t+\Delta t_S} {}^{t+\Delta t}f_i^S \delta u_i^S {}^{t+\Delta t}dS \quad (6.1)$$

Where l.h.s is the total internal virtual work and r.h.s is total external virtual work. The ${}^{t+\Delta t}\tau_{ij}$ are the Cartesian components of the Cauchy stress tensor, the ${}^{t+\Delta t}e_{ij}$ are the Cartesian components of an infinitesimal strain tensor, the ${}^{t+\Delta t}f_i^B$ and ${}^{t+\Delta t}f_i^S$ are the components of the externally applied body and surface force vectors, respectively, and δu_i is the i th component of the virtual displacement vector.

6.2 Newton-Raphson Algorithm

Substituting the element coordinate and displacement interpolation into the principle of virtual work expression Eq.(6.1), the equilibrium equation can be written as

$${}^{t+\Delta t}\mathbf{R} - {}^{t+\Delta t}\mathbf{F} = 0 \quad (6.2)$$

where the vector ${}^{t+\Delta t}\mathbf{R}$ lists the externally applied nodal point forces in the configuration at time $t + \Delta t$, and the vector ${}^{t+\Delta t}\mathbf{F}$ lists the nodal point forces that correspond to the element stresses in this configuration. For the nonlinear problems, the basic approach for an incremental step-by-step solution is to assume that the solution for the discrete time t is known, and that the solution for the discrete time $t + \Delta t$ is required, where Δt is a suitably chosen time increment. Hence, considering (6.2) at time $t + \Delta t$ we have

$$\mathbf{f}(\mathbf{U}^*) = 0 \quad (6.3)$$

where
$$\mathbf{f}(\mathbf{U}^*) = {}^{t+\Delta t}\mathbf{R}(\mathbf{U}^*) - {}^{t+\Delta t}\mathbf{F}(\mathbf{U}^*) \quad (6.4)$$

Assume that in the iterative solution we have evaluated ${}^{t+\Delta t}\mathbf{U}^{(i-1)}$; then a Taylor series expansion gives

$$\mathbf{f}(\mathbf{U}^*) = \mathbf{f}({}^{t+\Delta t}\mathbf{U}^{(i-1)}) + \left[\frac{\partial \mathbf{f}}{\partial \mathbf{U}} \right]_{{}^{t+\Delta t}\mathbf{U}^{(i-1)}} (\mathbf{U}^* - {}^{t+\Delta t}\mathbf{U}^{(i-1)}) \quad (6.5)$$

where higher-order terms are neglected. Substituting from (6.4) into (6.5) and using (6.3) we obtain

$$0 = {}^{t+\Delta t}\mathbf{R} - {}^{t+\Delta t}\mathbf{F}^{(i-1)} + \left[\frac{\partial \mathbf{R}}{\partial \mathbf{U}} - \frac{\partial \mathbf{F}}{\partial \mathbf{U}} \right]_{{}^{t+\Delta t}\mathbf{U}^{(i-1)}} (\mathbf{U}^* - {}^{t+\Delta t}\mathbf{U}^{(i-1)}) \quad (6.6)$$

when we assume that the externally applied loads are independent of the displacements,

which means $\left. \frac{\partial \mathbf{R}}{\partial \mathbf{U}} \right|_{{}^{t+\Delta t}\mathbf{U}^{(i-1)}} = 0$, (6.6) becomes

$$\left[\frac{\partial \mathbf{F}}{\partial \mathbf{U}} \right]_{t+\Delta t, \mathbf{U}^{(i-1)}} (\mathbf{U}^* - {}^{t+\Delta t} \mathbf{U}^{(i-1)}) = {}^{t+\Delta t} \mathbf{R} - {}^{t+\Delta t} \mathbf{F}^{i-1} \quad (6.7)$$

We now define

$$\Delta \mathbf{U}^{(i)} = \mathbf{U}^* - {}^{t+\Delta t} \mathbf{U}^{(i-1)} \quad (6.8)$$

and

$$\left. \frac{\partial \mathbf{F}}{\partial \mathbf{U}} \right|_{t+\Delta t, \mathbf{U}^{(i-1)}} = {}^{t+\Delta t} \mathbf{K}^{(i-1)} \quad (6.9)$$

where ${}^{t+\Delta t} \mathbf{K}^{(i-1)}$ is the tangent stiffness matrix in iteration $i-1$, which we assume to be nonsingular. Thus (6.7) can be written as

$${}^{t+\Delta t} \mathbf{K}^{(i-1)} \Delta \mathbf{U}^{(i)} = {}^{t+\Delta t} \mathbf{R} - {}^{t+\Delta t} \mathbf{F}^{(i-1)} \quad (6.10)$$

Since (6.5) represents only a Taylor series approximation, the displacement increment correction is used to obtain the next displacement approximation

$${}^{t+\Delta t} \mathbf{U}^{(i)} = {}^{t+\Delta t} \mathbf{U}^{(i-1)} + \Delta \mathbf{U}^{(i)} \quad (6.11)$$

The relation in (6.9) and (6.10) constitute the Newton-Raphson solution of (6.2).

6.3 Three Types of Modeling

Three different models, i.e. for bending, pressure loading and frictional contact, are derived respectively.

6.3.1 Tube Bending Modeling

Based on the kinematics and constitutive equation discussed in Chapter 3 and Chapter 4, the principle of virtual work is used to satisfy equilibrium and takes the following form:

$$\sum_{i=1}^I \int_{A^i} (\sigma_x^i \delta \varepsilon_x^i + \sigma_{s_i}^i \delta \varepsilon_{s_i}^i) dA^i + \sum_{j=1}^J \lambda_j \delta C_j = T \delta \varepsilon_x^0 \quad (6.12)$$

where I is the number of segments in the cross-section, J is the number of constraint equations, λ_j are Lagrange multipliers, C_j are the constraint equations (from Eqs.(3.12-3.14), T is the tension (compression) applied, $dA^i = ds_i dz_i$ for the straight segment or $dA^i = R^i d\phi_i dz_i$ for arcs.

The displacement component w_i, u_i for each straight segment are approximated using the following Fourier series expressions:

$$w_i = \alpha_0^i + \sum_{n=1}^{N^i} \alpha_n^i \cos \frac{n\pi s_i}{l_i^0} + \sum_{n=1}^{N^i} \beta_n^i \sin \frac{n\pi s_i}{l_i^0} \quad (6.13a)$$

$$u_i = \gamma_0^i + \sum_{n=1}^{N^i} \gamma_n^i \cos \frac{n\pi s_i}{l_i^0} + \sum_{n=1}^{N^i} \delta_n^i \sin \frac{n\pi s_i}{l_i^0} \quad (6.13b)$$

while for an arc, they are given by

$$w_i = \alpha_0^i + \sum_{n=1}^{N^i} \alpha_n^i \cos \frac{n\pi \phi_i}{\Delta \phi^i} + \sum_{n=1}^{N^i} \beta_n^i \sin \frac{n\pi \phi_i}{\Delta \phi^i} \quad (6.14a)$$

$$u_i = \gamma_0^i + \sum_{n=1}^{N^i} \gamma_n^i \cos \frac{n\pi \phi_i}{\Delta \phi^i} + \sum_{n=1}^{N^i} \delta_n^i \sin \frac{n\pi \phi_i}{\Delta \phi^i} \quad (6.14b)$$

After substituting from Eqs.(6.13a-b) and (6.14a-b) into the principle of virtual work Eq.(6.12), a nonlinear expression of the following form will result

$$\mathbf{f}(\mathbf{c}, \kappa_Y, \kappa_Z, T) = 0 \quad (6.15a)$$

$$\text{where } \mathbf{c} = \{\alpha_0^i, \alpha_n^i, \beta_n^i, \gamma_0^i, \gamma_n^i, \delta_n^i, \epsilon_x^0, \lambda_j\} \quad (6.15b)$$

Eq.(6.15) should be solved for \mathbf{c} for given values of $d\kappa_Y, d\kappa_Z$ and dT .

Since Eq.(6.15) is highly nonlinear, it will be numerically solved by the Newton-Raphson method. The Newton-Raphson iterative method used to solve \mathbf{c} will look like this:

$$[K][d\bar{c}] = [R] = F_{Ext} - F_{Int} \quad (6.16)$$

where \mathbf{K} is the stiffness matrix, $\delta\bar{c}$ is the incremental \bar{c} and \mathbf{R} is the force residual.

F_{Ext} is externally applied nodal forces, F_{Int} is the nodal forces that correspond to the element stress in this configuration (Internal forces).

6.3.2 Pressure Loading Modeling

Pressure loading is modeled as an external force to expand the tube. The external work done by a pressure p applied to the inside of the tube is equal to

$$\delta W_{Ext}^p = \sum_{i=1}^I \int_{A_p^i} p \hat{n}^i \delta(\Delta u^i) dA_p^i = \sum_{i=1}^I \int_{A_p^i} p \hat{n}^i \frac{\partial(\Delta u^i)}{\partial \bar{c}} \delta \bar{c} dA_p^i \quad (6.17)$$

where $\delta(\Delta u^i)$ is the virtual displacement increment having two components $\delta(\Delta w^i)$ and $\delta(\Delta v^i)$, \hat{n}^i is the unit outward normal to the surface A_p^i .

The principle of virtual work for bending and pressure loading modeling becomes

$$\sum_{i=1}^I \int_{A^i} (\sigma_x^i \delta \varepsilon_x^i + \sigma_{s_i}^i \delta \varepsilon_{s_i}^i) dA^i + \sum_{j=1}^J \lambda_j \delta C_j = T \delta \varepsilon_x^o + \sum_{i=1}^I \int_{A_p^i} p \hat{n}_i \delta(\Delta u^i) dA_p^i \quad (6.18)$$

The variation of the virtual external work due to internal pressure loading is

$$F_{Ext}^p = p \sum_{i=1}^I \int_{A_p^i} \hat{n}^i \frac{\partial(\Delta u^i)}{\partial \bar{c}} dA_p^i \quad (6.19)$$

Due to the follower forces effect (Hibbitt, 1979), the load stiffness matrix is

$$\begin{aligned} K_{Ext}^p &= p \sum_{i=1}^I \int_{A_p^i} \left(\frac{\partial(\hat{n}^i)}{\partial \bar{c}} \frac{\partial(\Delta u^i)}{\partial \bar{c}} + \hat{n}^i \frac{\partial^2(\Delta u^i)}{\partial^2 \bar{c}} \right) dA_p^i \\ &= p \sum_{i=1}^I \int_{A_p^i} \frac{\partial(\hat{n}^i)}{\partial \bar{c}} \frac{\partial(\Delta u^i)}{\partial \bar{c}} dA_p^i \end{aligned} \quad (6.20)$$

Eq. (6.19) and (6.20) will appear on the right-hand and left-hand side of the Newton-Raphson expression (Eq. (6.16)) respectively, namely,

$$\left[\underline{\underline{K}} + \underline{\underline{K}}_{Ext}^p \right] \left[d \underline{\underline{c}} \right] = \left[\underline{\underline{R}} \right] = \underline{\underline{F}}_{Ext} + \underline{\underline{F}}_{Ext}^p - \underline{\underline{F}}_{Int} \quad (6.21)$$

When we implemented above formulations into the code, we found that the load stiffness matrix $\underline{\underline{K}}_{Ext}^p$ has nearly no effects on the solution which led us to simplify the formulation. Actually, if we approximated $\hat{n}^i \delta(\Delta \underline{\underline{u}}^i) \approx \delta(\Delta \underline{\underline{w}}^i)$, the whole formulation above can be simplified. The proof can be seen in Appendix B. Since $\frac{\partial^2(\Delta \underline{\underline{w}}^i)}{\partial^2 \underline{\underline{c}}} = 0$, there will be no stiffness matrix due to pressure ($\underline{\underline{K}}_{Ext}^p$) going to the left side of the Newton-Raphson expression (Eq.(6.21)). Both methods are implemented in the code, the results are almost the same.

6.3.3 Frictional Contact Modeling

The most challenging task when developing a numerical code for metal forming processes is to model frictional contact. To model the tooling-workpiece frictional contact correctly, the following two conditions must be continually checked during each equilibrium iteration:

1. Penetration of the workpiece nodes into the tooling.
2. Nodal contact forces becoming tensile at the contact boundary (separation).

Once the penetration of the workpiece nodes into the tooling has been detected, the penetration nodes must be returned to the tooling surface and constrained to stay on the

tooling surface for the remainder of the equilibrium iterations. The nodes, which are returned to the tooling surface, are constrained to move only tangent to the tooling surface and only condition 2 stated above can cause a contacting node to be detached from the tooling surface. Figure 6.1 shows an example of a typical contact check during the Newton-Raphson equilibrium iteration.

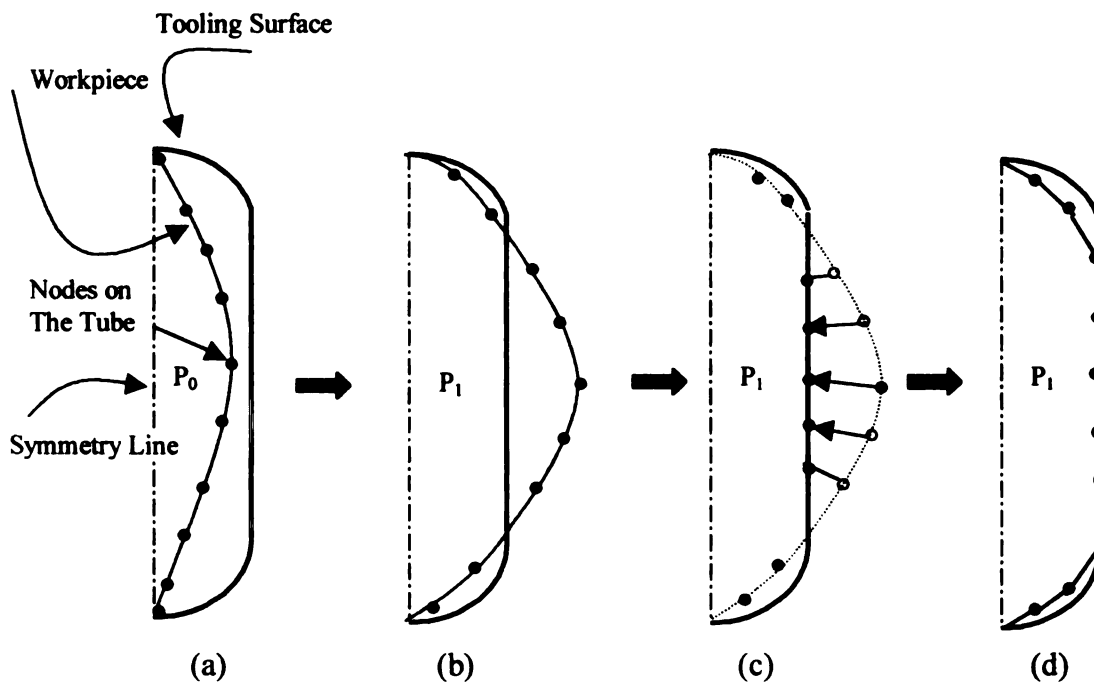


Figure 6.1 A schematic of tool-workpiece contact check

(a) shows the tube and the tooling, (b) shows initial penetration of some of the nodes, (c) shows how those nodes are returned to the tooling surface and finally (d) shows how the equilibrium shape is obtained after several iterations.

The external work done by the frictional contact is added into the virtual work principle equation (6.12) as following:

$$\sum_{i=1}^I \int_{A_i} (\sigma_x^i \delta \epsilon_x^i + \sigma_s^i \delta \epsilon_s^i) dA^i + \sum_{j=1}^J \lambda_j \delta C_j = T \delta \epsilon_x^0 + \sum_{i=1}^I P \hat{n}_i \delta(\Delta u^i) dA_p^i + \sum_{i=1}^I \int_{A_r^i} \tau_i \delta(\Delta u^i) dA_r^i \quad (6.22)$$

where τ_i is the traction on the surface of the tube and $\delta(\Delta u^i)$ is the virtual incremental displacement of the contacting nodes.

In order to improve convergence, a special algorithm is introduced (see Figure 6.2). For each trial set of contacting and non-contacting nodes, equilibrium iteration is performed. After equilibrium is satisfied, the nodes are reexamined for non-penetration condition. The contact set is then updated by releasing or projecting certain nodes and another equilibrium iteration is initiated.

In each contact iteration, the trial displacements are first updated according to the Newton-Raphson procedure and the non-penetration contact condition is then applied to these trial values by projecting the contact nodes to the tool surface along the normal vector. The modified trial solutions are used for Newton-Raphson iteration. Within this force equilibrium iteration, the internal force is calculated. The signs of the sheet normal force at contact points are checked so that the nodes having non-compressive force are released.

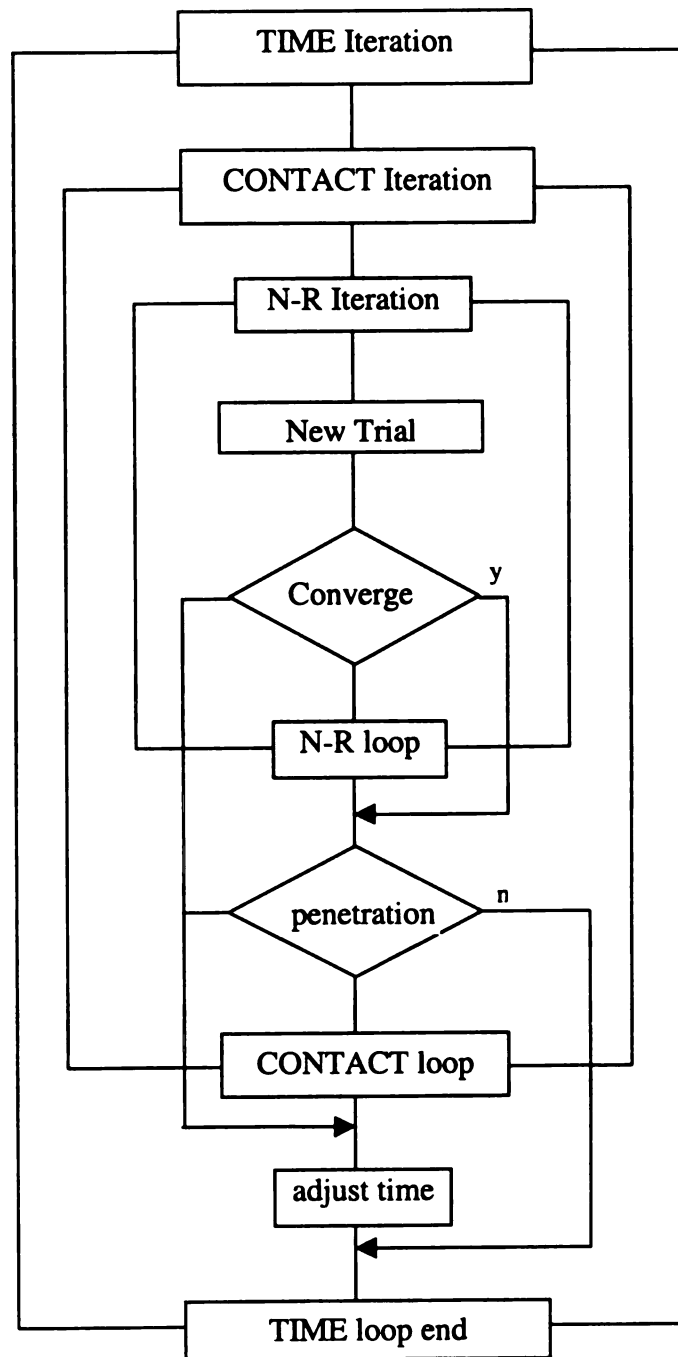


Figure 6.2 Flow chart for contact iteration

CHAPTER 7

PROGRAM STRUCTURE

The program includes input file, main program and output files.

7.1 Input File

The input is divided into two parts. The first part contains all the geometric, numerical and material information for a run. It is written in an input file that is read by the program prior to specification of the loading. The second part contains the loading history. This input is provided interactively by the user. All input is free-formatted.

7.1.1 Geometric, Numerical and Material Input

1. Title of this case

TITLE

TITLE: Array of 72 characters used to identify a case.

2. Number of nodes

NODE

NODES: Number of nodes in the cross-section. Each segment in the cross-section is bounded by two nodes. Maximum: 20.

3. Node coordinates. Input this record NODES times before proceeding to 4.

YN,ZN

YN: Y global coordinate of the location of this node.

ZN: Z global coordinate of the location of this node.

4. Number of segments.

NSEG, MU, DELTAV

NSEG: Total number of segments in the cross-section. The segment may be straight lines or circular arcs. Maximum: 40.

MU: The frictional factor.

DELTA V: The relative sliding velocity

5. **Type of segment.** Input NSEG item {5,6} pairs before proceeding to 7.

STYPE

STYPE: Enter str if the segment being described is straight or arc if it is a circular arc.

6. **Segment parameters.**

For straight segments input the following record:

INODE, JNODE, T, NCOEFF, IS, IZ

INODE: First node of the segment ($s=0$).

JNODE: Second node of the segment ($s=l_0$).

T: Thickness of the segment (t).

NCOEFF: Number of terms in the Fourier series expansions for the displacement components(N). Maximum: 10. Recommended: 4 to 6.

IS: Number of Gauss integration points along the segment. Maximum: 48.
Recommended: 8 to 12.

IZ: Number of Gauss integration points along thickness of the segment. Maximum: 48. Recommended: 3 to 7.

For arc segments input the following record:

INODE, JNODE, T, NCOEFF, IS, IZ, YC, ZC, IAO

INODE: First node of the segment ($\phi=0$).

JNODE: Second node of the segment ($\phi=\Delta\phi$). **INODE** and **JNODE** must be chosen so that the coordinate ϕ has a counterclockwise direction.

T: Thickness of the segment (t).

NCOEFF: Number of terms in the Fourier series expansions for the displacement components(N). Maximum: 10. Recommended: 4 to 6.

IS: Number of Gauss integration points along the segment. Maximum: 48. Recommended: 8 to 12.

IZ: Number of Gauss integration points along thickness of the segment. Maximum: 48. Recommended: 3 to 7.

YC: Y-coordinate of the center of the arc(Y_c).

ZC: Z-coordinate of the center of the arc(Z_c).

IAO: Input a if $\Delta\phi \leq \pi$ rad., input o if $\Delta\phi > \pi$ rad.

7. Number of point constraints

NPC

NPC: Number of point constraints. At least three constraints are needed to prevent rigid body motion. Also input the constraints needed to maintain contact with the mandrel or symmetry conditions. All constraints are enforced at nodes.

8. Point constraint information. Input this record **NPC** times before proceeding to 9.

NSPC, IVARPC

NSPC: Segment number for which the point constraint will be enforced.

- If **NSPC** is positive, the constraint is enforced at the node with $s = 0$ or $\phi = 0$.
- If **NSPC** is negative, the constraint is enforced at the node with $s = l_0$ or $\phi = \Delta\phi$.

IVARPC: Variable which will be constrained.

- To constrain the rotation β , input 1.
- To constrain the displacement component u , input 2.
- To constrain the displacement component w , input 3.

9. Iteration parameters:

TOL, ITEMAX, JEVAL

TOL: Convergence tolerance of Newton-Raphson iteration. Recommended:0.0001.

ITEMAX: Maximum allowable number of iterations.

JEVAL: Multiple of the iteration count at which the Jacobian is evaluated. If **JEVAL** = 1 the Jacobian is evaluated every iteration, If **JEVAL** = 2 it is evaluated every other iteration, etc.

10. Material properties.

E, V, SIGMY, R, XK, XN, EPS0

E: Young's modulus.

V: Poisson's ratio.

SIGMY: Initial yield stress.

R: Anisotropy parameter.

XK: Material constant.

XN: Hardening exponent.

ESP0: Initial plastic strain.

11. Input / Output options.

IWR, IZSYMM

IWR:

- **IWR** = 1: print coefficients and Lagrange multipliers.

- **IWR = 0**: do not print coefficients and Lagrange multipliers.

IZSYMM: This variable indicates whether the cross-section defined by the input above is a whole section or on-half of a symmetric section. The value of **IZSYMM** affects input / output operations only.

- **IZSYMM = 1**: the cross-section is symmetric about the Z axis.
- **IZSYMM = 0**: no symmetry about the Z axis exists.

7.1.2 Loading Input

The input of the loading parameters is interactive. Loading is prescribed in an incremental manner. The loading record below may be repeated as many times as necessary.

Loading parameters

NINC, CZINC, CYINC, TINC, PINC

NINC: Number of increments. Input 0 to stop execution.

CZINC: Increment size of the variable κ_z . Note that the sign of **CZINC** must be decided by the location of the mandrel. For example, **CZINC** must be negative for the case shown in Fig.4.1.

CYINC: Increment size of the variable κ_y . This will usually be zero.

TINC: Tension increment.

PINC: Internal pressure increment.

7.2 Program Flow Chart

The program includes a main program and 24 subroutines.

Subroutine **input**: input geometric and material parameters.

Subroutine **store**: store integration, trigonometric and second derivative information.

Subroutine **newrap**: solve system of nonlinear equations using Newton-Raphson method.

Subroutine **build**: evaluate the system of equation and the jacobian.

Subroutine **constr**: add constraint contribution to system of equation and jacobian matrix.

Subroutine **decomp**: find the inverse matrix using Gauss-Jordan method.

Subroutine **disp**: evaluate displacements and their derivatives with respect to s at integration points along a segment.

Subroutine **dstrn** and **dstrnC**: derivatives of displacement components and their derivatives with respect to the coefficients of the series expansions at one point along s for straight and arc segment respectively.

Subroutine **d2curvature**: evaluate the second derivatives of curvature.

Subroutine **incm**: increment of all variables.

Subroutine **solve**: solve the nonlinear equations.

Subroutine **stndsp**: find strains at the integration points along the local coordinate.

Subroutine **stsstn**: find stress increments and force residual at integration points.

Subroutine **cnstutv**: constitutive equation.

Subroutine **contact**: deal with contact problem.

Subroutine **coloumb**: use Coloumb friction model.

Subroutine **dieinfo**: calculate die geometric information.

Subroutine **forcecheck**: check nodal force at each contact point.

Subroutine **getcoord**: calculate the coordinates of each integration point.

Subroutine **nodalf**: calculate nodal force at each contact point.

Subroutine **setpenalty**: set penalty function.

Subroutine **violation**: check each integration point to see if it violate contact.

Subroutine **bringback**: bring each contact point to die surface.

Following is the flow chart of the program:

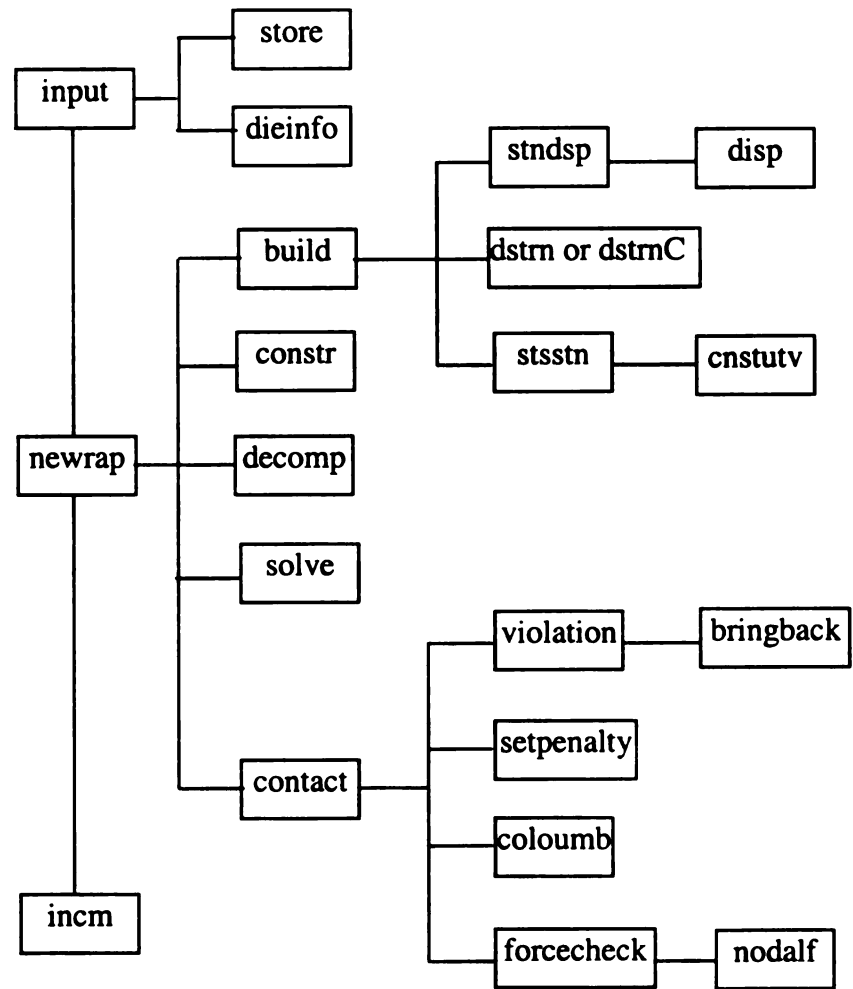


Figure 7.1 Flow chart of the program

7.3 Output File

The program has three output files: `betges.out`, `betges.mk`, `betges.coeff`. The contents of each file are described below:

betges.out: This file is formatted and contains the output of the program in the form of tables. The first part of this file is written prior to the specification of the loading and contains an augmented echo print of the input. It is useful to look at this part of the file to ensure that the input file was read correctly. The second part includes a list of the curvature, axial strain, bending moments, tension and internal pressure at each loading step. If the variable **IWR** is set to 1 then the file will also contain the coefficients of the trigonometric series expansions for each segment. If the variable **IZSYMM** is set to 1 then the value of T and M_Y are reported for the full section, while M_Z is set to zero.

betges.mk: This file contains one line per loading step containing the value of the following parameters:

$$\kappa_Z, \kappa_Y, \varepsilon_x^0, M_Y, M_Z, T, P$$

betges.coeff: This file contains information necessary to make plot of the deformed cross-section of the member at any loading step. It also contains information to plot the shape of the cross-section prior to loading. The file is organized as follows:

Line 1: (Format: i2)

Number of segments.

For each segment, the file contains the next set of three records:

Line 2.1: (i3, e13.5, a4, 3e13.5)

Number of terms in this segment, length of the segment, type of segment, location of the segment in Y , location of the segment in Z , radius of the segment. For straight segments, the location of the segment is partially given by the coordinates Y_0 and Z_0 as shown in Figure 3.2. The radius is assigned a value of one. For arc segments, the length of the segment is in angular measure, the location of the segment is partially given by the coordinates of the center Y_c and Z_c as shown in Figure 3.3.

Line 2.2: (4e13.5)

Coordinates of the nodes bounding this segment in the following order: Y -coordinate of first node, Z -coordinate of first node, Y -coordinate of second node, Z -coordinate of second node.

Line 2.3: (2e13.5)

Sine and cosine of the angle θ defined in Figure 3.2 for straight segments. For arcs, $\sin \theta = \cos \phi_0$ and $\cos \theta = -\sin \phi_0$, where ϕ_0 is defined in Figure 3.3.

This concludes the part of this file which contains the original, undeformed description of the cross-section. The second part of the file contains, for each loading step, additional information necessary to describe the deformed shape of the cross-section. For each loading step, the file contains the following:

Line 3.1: (i2)

Step number.

Line 3.2: (i2)

Segment number.

For each segment in the cross-section the output file contains the following set of four records:

Line 3.3.1: (6(e22.14))

$\alpha_0, (\alpha_n, n = 1, \text{number of terms}).$

Line 3.3.2: (6(e22.14))

$(\beta_n, n = 1, \text{number of terms}).$

Line 3.3.3: (6(e22.14))

$\gamma_0, (\gamma_n, n = 1, \text{number of terms}).$

Line 3.3.4: (6(e22.14))

$(\delta_n, n = 1, \text{number of terms}).$

CHAPTER 8

EXAMPLES

There are several examples shown in this chapter, including stretch-bending, expansion under internal pressure and contact example.

8.1 Bending Examples

Example 1 : Stretch-bending a tube with rectangular cross-section

This example concerns a tube with rectangular cross-section. The section is 1.97 in. wide and 1.18 in. high (outside dimensions). The wall thickness is 0.07 in. See Figure 8.1. The material properties in plasticity implementation $\sigma = K(\epsilon + \epsilon_0)^N$ are: $E = 10 \times 10^6$ psi, $\nu = 0.33$, $\sigma_y = 5,500$ psi, $R=0.7$, $K = 64 \times 10^3$ psi, $\epsilon_0 = 0.0$ and $N = 0.25$.

The input file used to run this case is shown below:

```
' Rectangular section '  
4  
0.950,0.555  
0.950,-0.555  
-0.950,-0.555  
-0.950,0.555  
4,0,0  
str  
1,2,0.070,4,8,3  
str  
2,3,0.070,4,8,3  
str  
3,4,0.070,4,8,3  
str  
4,1,0.070,4,8,33  
1,2  
1,3  
-1,3  
0.0001,20,1  
1.e7,0.33,5500.,0.7,64000.,.25,0.0  
0,0
```

The loading history consisted of the following

1. Apply tension to 4200 lbs.
2. Bend to a radius of 20 in.

The interactive input records were as follows:

21, 0., 0., 200., 0.

100, -0.0005, 0., 0.

Example 2: Stretching / bending a tube with circular cross-section

This example concerns a tube with circular cross-section. The diameter is 0.6092 in. The wall thickness is 0.0356 in. See Figure 8.2.

The material properties(aluminum-alloy $\sigma = K(\varepsilon + \varepsilon_0)^N$) are $E = 10.295 \times 10^6$ psi, $\nu = 0.3$, $\sigma_y = 19,618$ psi, $R = 1.0$, $K = 83,634$ psi and $N = 0.3593$, $\varepsilon_0 = 0.01658$.

The final state is $\kappa = 0.064 \text{ in}^{-1}$ and $T = 1000$ lb.

The input file used to run this case is shown below:

```
'Circular case'
2
0., 0.6092
0., -0.6092
1, 0.1, 0.0001
arc
1, 2, 0.0356, 6, 12, 7, 0., 0., a
5
1, 1
1, 2
1, 3
-1, 1
-1, 2
0.0001, 20, 1
10.295e6, 0.3, 19618, 1.0, 83634, 0.3593, 0.01658
0, 1
```

Example 3: Bending a tube with circular cross-section to collapse

Figure 8.3 shows example of bending a tube to collapse. The material and dimension are similar to the one in example 2.

8.2 Free Expansion Case

Example 4: Formulated, implemented and tested the internal pressure loading and expansion of the tube.

Figures 8.4 shows examples of expanding symmetric tube with internal pressure. The material and dimension are similar to the one in example 2. Final internal pressure is 3,000 psi.

Same example was run in ABAQUS by using 3D shell element. Maximum hoop strain are 16% and 18%, axial strain are -8% and -9% and the change of diameter are 0.183in and 0.2in, in this 2D-Hydroforming code and ABAQUS respectively. It shows that results are in good agreement.

8.3 Contact Examples

Example 5: A round aluminum tube expanded into a square die with sharp-corners.

Final internal pressure is 7,000 psi, material is similar to aluminum-alloy in example 2.

Final shape is seen in Figure 8.5a. Compared with the results of ABAQUS(see Figure 8.5b). The final shape is in good agreement. Twenty-six S4 shell elements were used in ABAQUS.

Example 6: Hoop strain distribution and intermediate shapes in a specialized contact example (Compared with GM experiment data)

The material properties (aluminum-alloy $\sigma = K(\varepsilon + \varepsilon_0)^N$) are $E = 10.3 \times 10^6$ psi, $\nu = 0.3$, $\sigma_y = 20,000$ psi, $R = 1.0$, $K = 63657$ psi and $N = 0.25$, $\varepsilon_0 = 0.0$.

Figure 8.6a shows hoop strain distribution and Figure 8.6b shows the intermediate shapes. Figure 8.7a-b are the experiment data of strain distribution.

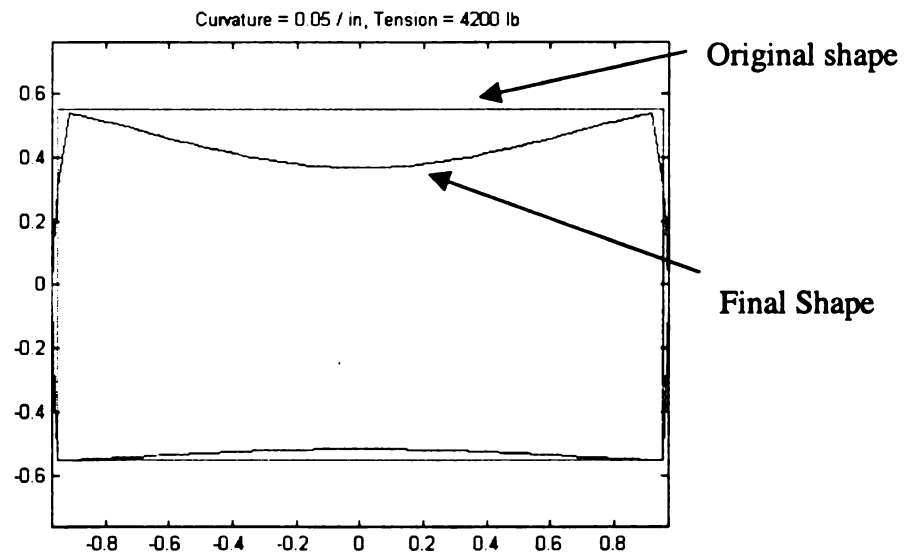


Figure 8.1 Stretching / bending of a rectangular section

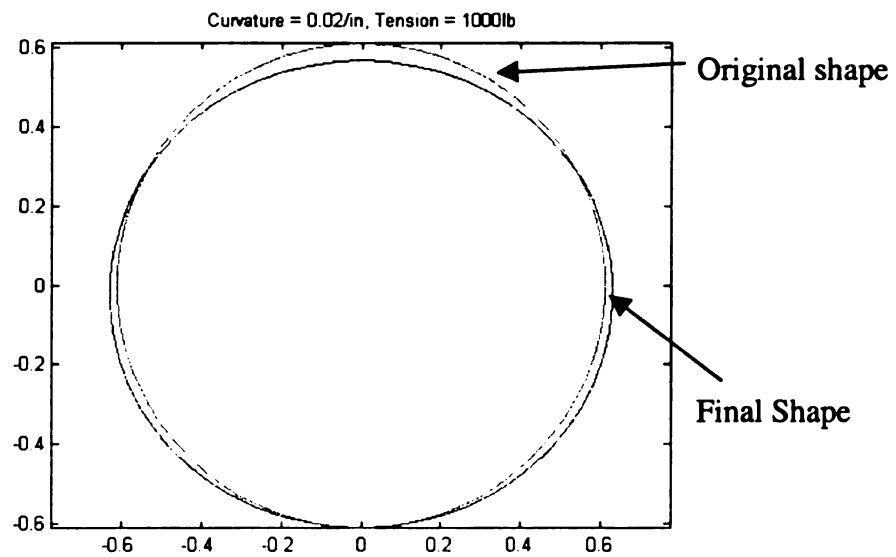


Figure 8.2 Stretching / bending of a circular section

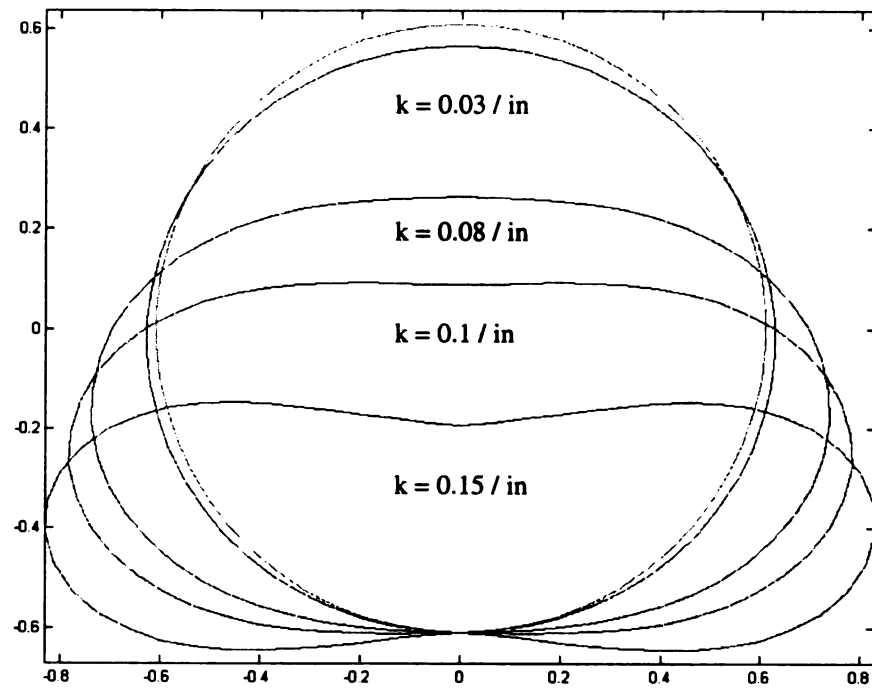
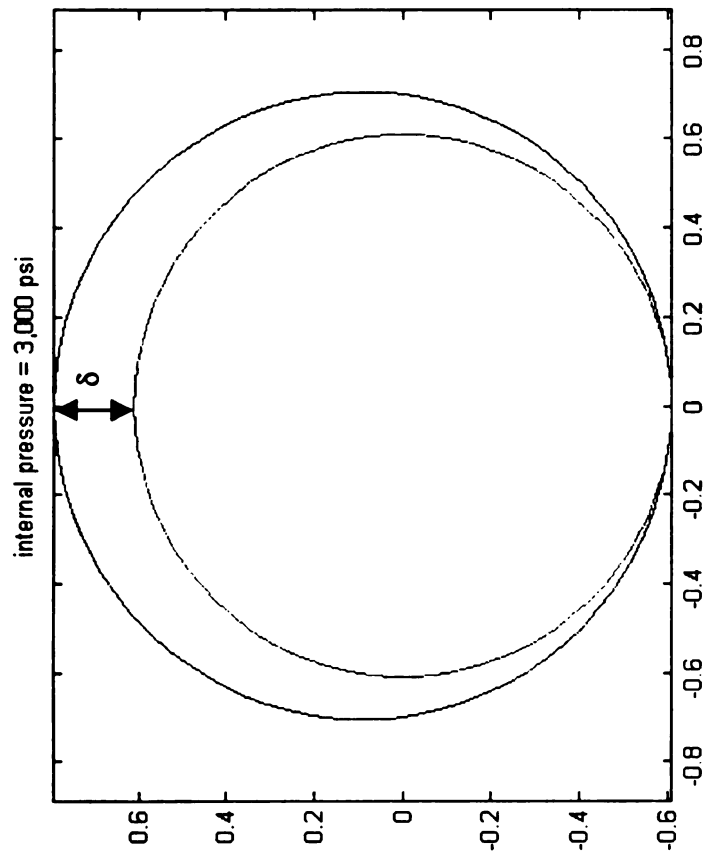


Figure 8.3 Bending a tube to collapse



Material Properties: $E = 10.295E06$ psi, $YS = 19618.5$ psi, $K = 83634$ psi, $\nu = 0.3$, $N = 0.3593$, $\epsilon_0 = 0.01658$
Loading: Pressure = 3,000 psi,
Geometry: Radius = 0.6092 inches, Thickness = 0.0356 inches

	2D-Hydroforming Code	ABAQUS
Max. Hoop Strain:	16%	18%
Axial Strain (feed):	-8%	-9%
δ	0.183"	0.2"

Figure 8.4 Strain and displacement result compared with ABAQUS

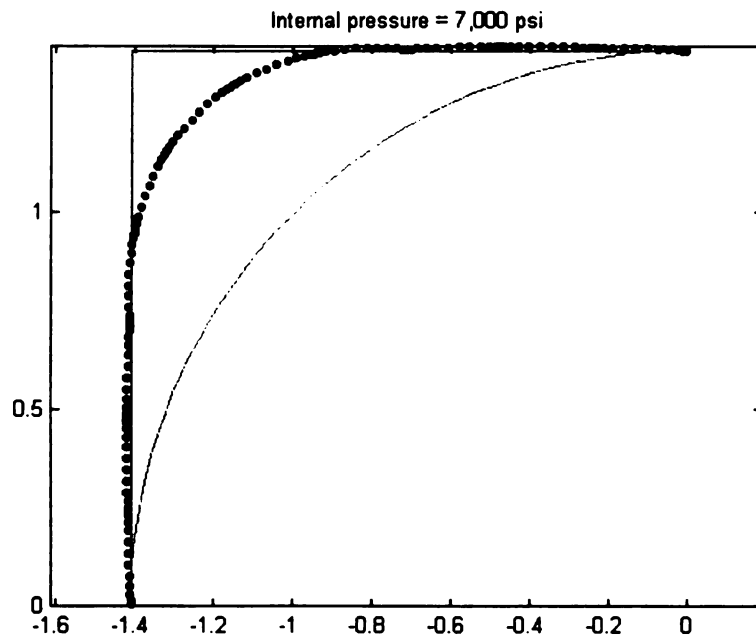


Figure 8.5a A round aluminum tube was expanded into a square die with sharp-corners

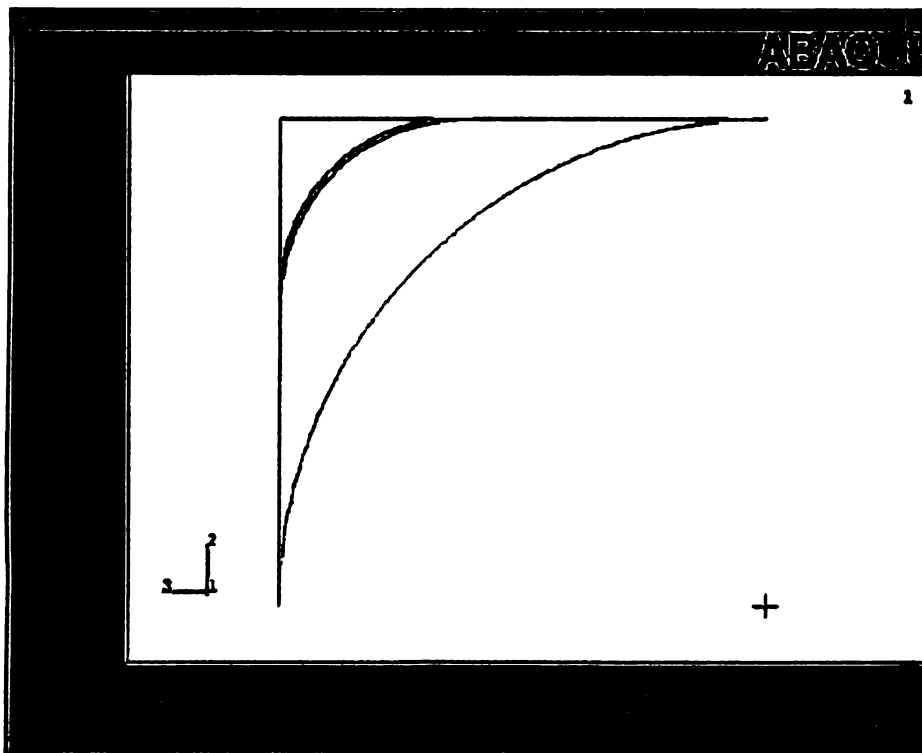
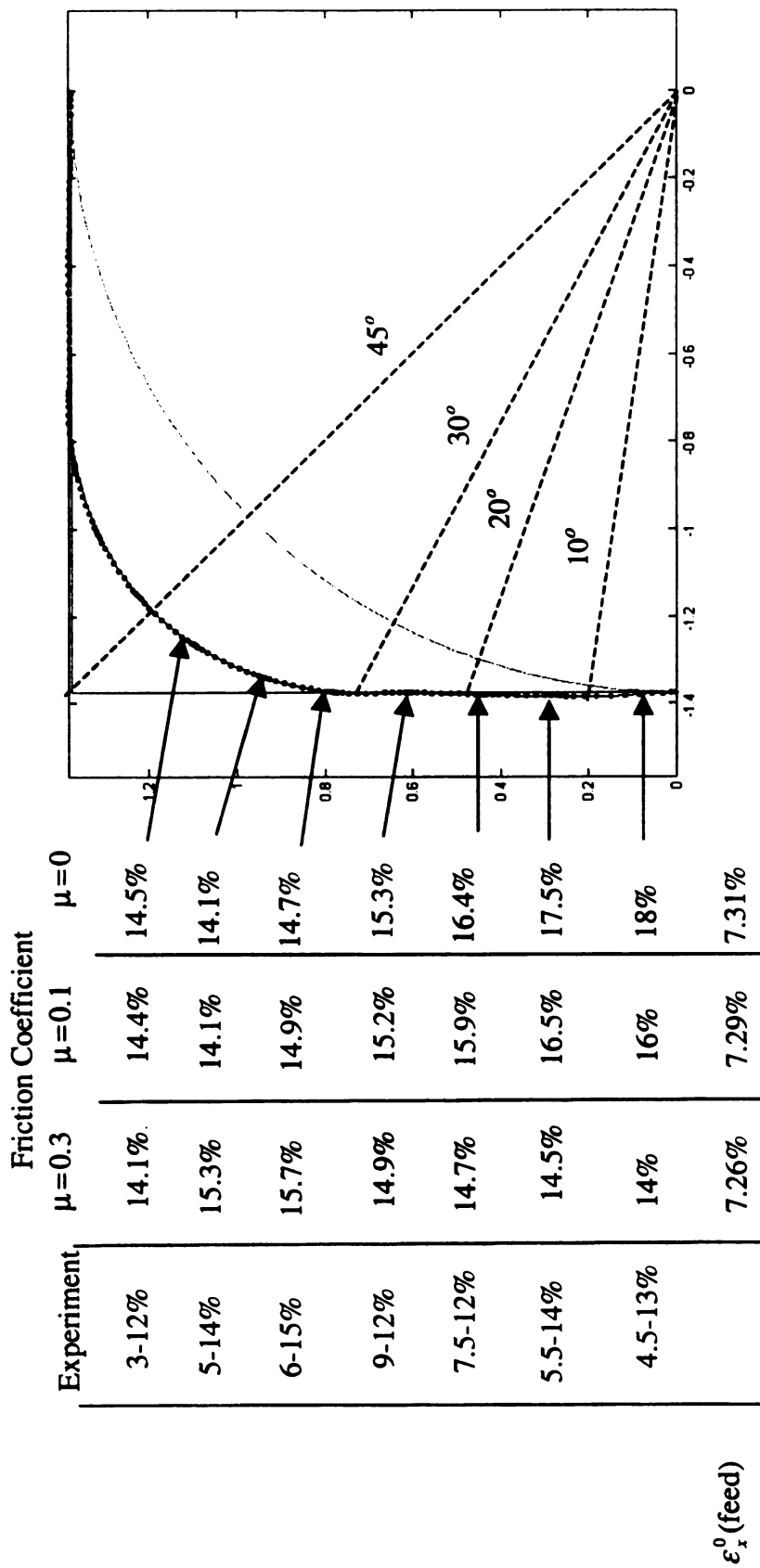


Figure 8.5b Final shape from ABAQUS



Material Properties: $E=10.3E06$ psi, $Y_S=20595$ psi, $K=57000$ psi, $\nu=0.3$, $N=0.273$, $\epsilon_0=0$
Loading: Pressure = 9,000 psi
Geometry: Radius of the Tube = 1.375 inches, Thickness = 0.1378 inches

Figure 8.6a Hoop strain distribution compared with experiment

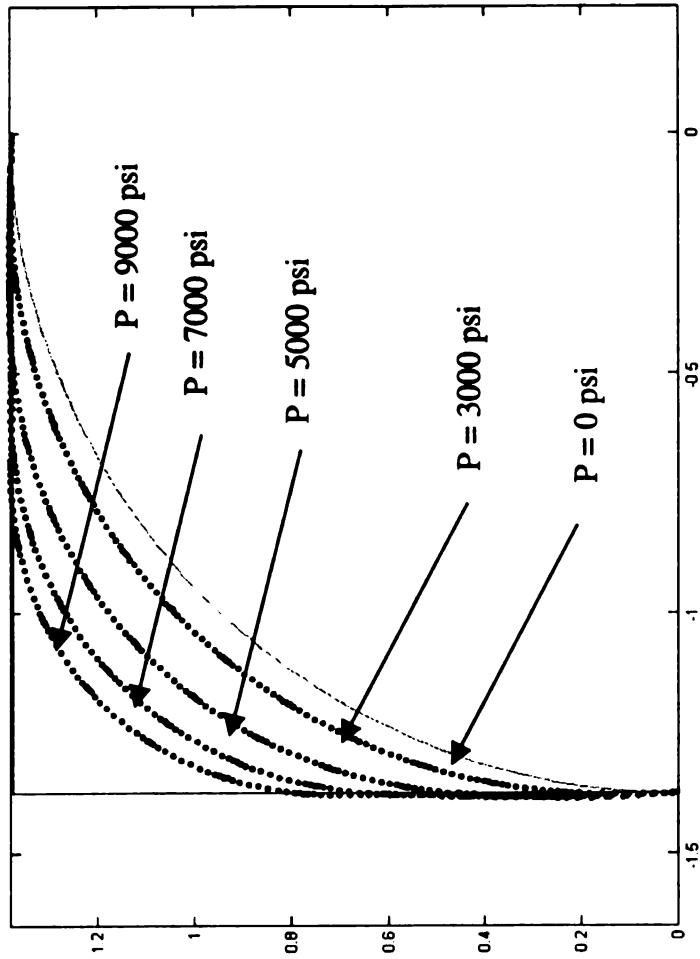


Figure 8.6b Intermediate Shapes of the Tube During Hydroforming

Material Model:

$$\sigma = K(\epsilon_0 + \epsilon)^N$$

Material Properties: $E=10.3E06$ psi, $YS=20595$ psi, $K=57000$ psi, $v=0.3$,

$N=0.273$, $\epsilon_0=0$,

Loading: Pressure = 3,000 psi, 5,000psi, 7,000 psi and 9,000 psi respectively

Geometry: Radius of the Tube = 1.375 inches, Thickness = 0.1378 inches

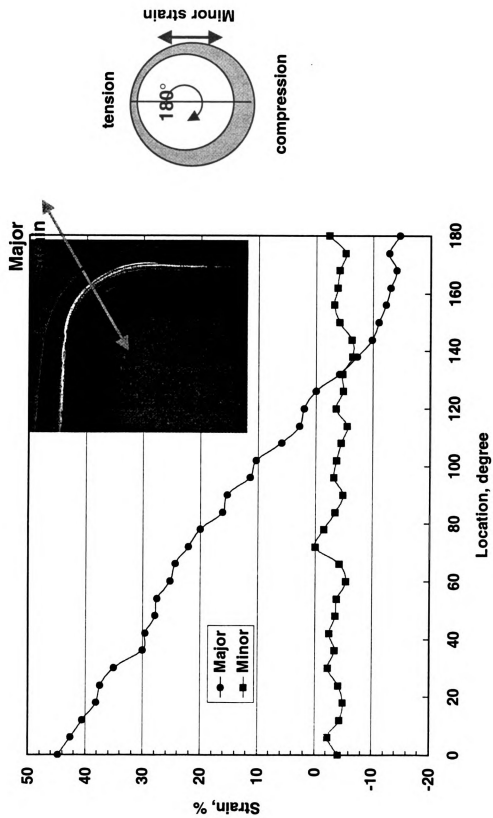


Figure 8.7 a Circumferential strain distribution after bending

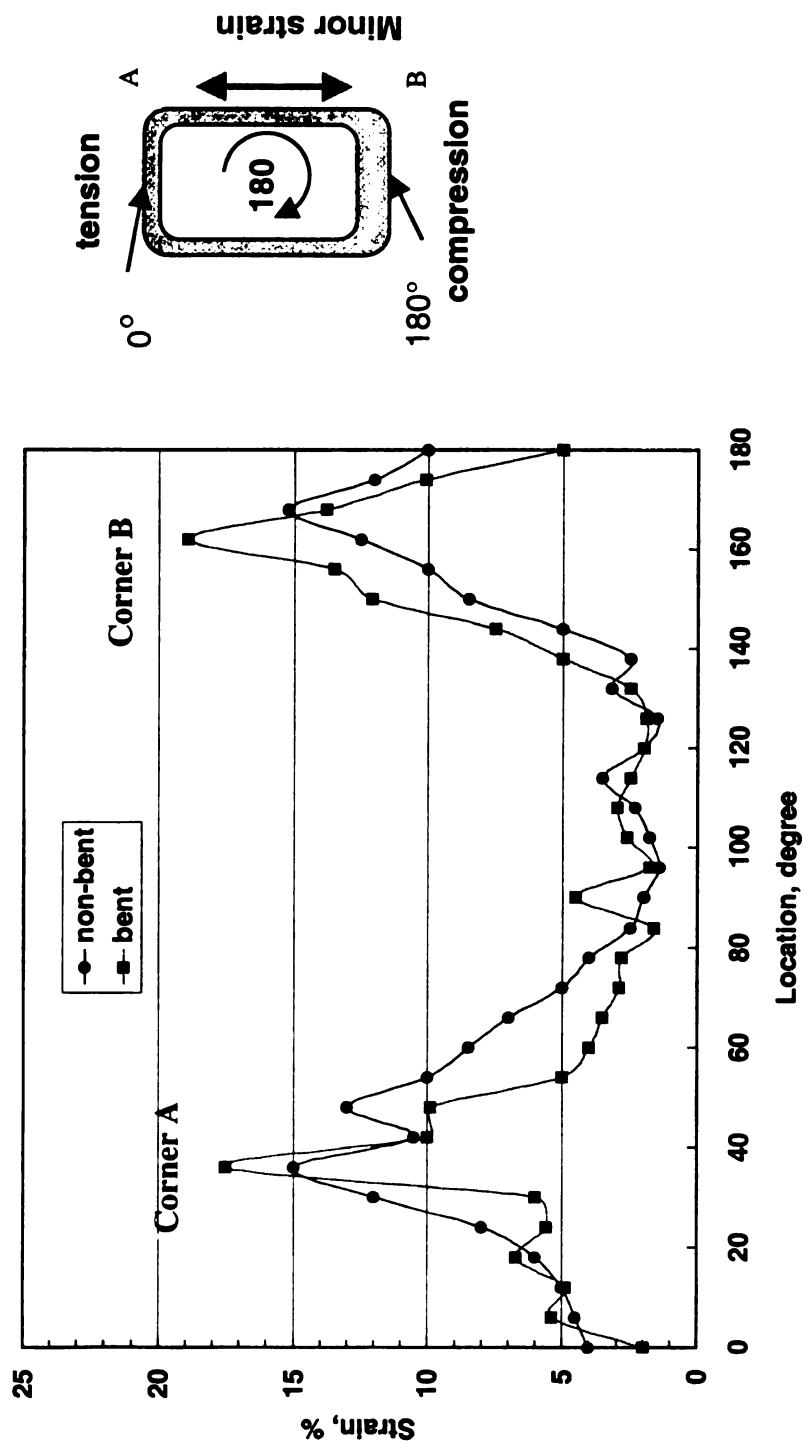


Figure 8.7b Circumferential strain distribution in hydroforming (9000psi)

CHAPTER 9

CONCLUSIONS

Based on the formulations presented in the thesis, a cross section analysis finite element code had been developed. This code is very efficient in calculating tube stretching and bending followed by hydroforming and expansion to fill the die in the hydroforming process. The code has been tested for several cases. The results from this 2D code were in good agreement with both commercial code ABAQUS and the limited experiment data available to us.

In the future, the failure model and instability (bifurcation, post-buckling etc) analysis will be implemented into the code. It is also planned to extend this code for the 3D analysis tube hydroforming process.

APPENDIX A

According to the total Lagrangian formulation discussed in Chapter 2 (Thin shell theory), we derived the membrane strain, rotation of normal vector and the current principal centerline curvature used in Chapter 3 (Kinematics) and compared with the formulation developed by Corona and Pourboghraat (1998) and Brush and Almroth (1975).

1. Membrane strain

For *straight segment*, the curvature $K_1=0$, then from Eq.(2.14) ,

$$\lambda_1 = [(1 + u_{,s})^2 + w_{,s}^2]^{\frac{1}{2}} = [1 + u_{,s}^2 + 2u_{,s} + w_{,s}^2]^{\frac{1}{2}} \quad (1)$$

Let's approximate the square root as:

$(1 + x)^{\frac{1}{2}} \approx 1 + \frac{1}{2}x - \dots$ for $x \ll 1$, Eq.(1) becomes:

$$\lambda_1 \approx 1 + u_{,s} + \frac{1}{2}u_{,s}^2 + \frac{1}{2}w_{,s}^2 \quad (2)$$

Since, $\lambda_1 = ds/dS$ and the engineering definition $e = \frac{ds - dS}{dS} = \frac{ds}{dS} - 1 = \lambda_1 - 1$

We have the membrane strain:

$$e \approx u_{,s} + \frac{1}{2}u_{,s}^2 + \frac{1}{2}w_{,s}^2 \quad (3)$$

which is used in Chapter 3 as Eq.(3.5) and Eq.(1.6) in Brush and Almroth (1975).

For *circular arc segment*, the undeformed shell is non-flat and has an initial curvature K_1 ,

then rearranging Eq.(2.14) and approximating the square root , we obtain

$$\lambda_1 \approx 1 + \frac{1}{2}[u_{,s}^2 + 2u_{,s} + K_1^2 w^2 - 2K_1 w - 2K_1 w u_{,s} + w_{,s}^2 + K_1^2 u^2 + 2K_1 u w_{,s}] ,$$

then membrane strain is

$$e \approx \frac{1}{2}(u_{,s}^2 + w_{,s}^2) + \frac{1}{2}K_1^2(u^2 + w^2) + u_{,s} + K_1(uw_{,s} - wu_{,s} - w) \quad (4)$$

Consider the circular arc segment shown in Figure 3.3 Since $Rd\phi = dS$, then

$$\frac{\partial(\cdot)}{\partial S} = \frac{1}{R} \frac{\partial(\cdot)}{\partial \phi} = K_1 \frac{\partial(\cdot)}{\partial \phi}, \text{ Eq.(4) becomes:}$$

$$\begin{aligned} e &\approx \frac{1}{2}K_1^2(u_{,\phi}^2 + w_{,\phi}^2) + \frac{1}{2}K_1^2(u^2 + w^2) + K_1u_{,\phi} + K_1(K_1uw_{,\phi} - K_1wu_{,\phi} - w) \\ &= \frac{1}{2}K_1^2[(u_{,\phi}^2 + w_{,\phi}^2) + (u^2 + w^2) + 2(uw_{,\phi} - wu_{,\phi})] + K_1(u_{,\phi} - w) \\ &= \left(\frac{u_{,\phi} - w}{R}\right)^2 + \frac{1}{2}\left(\frac{u + w_{,\phi}}{R}\right)^2 + \frac{1}{2}\left(\frac{w - u_{,\phi}}{R}\right)^2 \end{aligned} \quad (5)$$

As shown in Figure 3.3, if the positive w direction is the opposite direction of the normal to the mid-surface vector, \hat{n} , then Eq.(5) becomes:

$$e = \left(\frac{u_{,\phi} + w}{R}\right)^2 + \frac{1}{2}\left(\frac{u - w_{,\phi}}{R}\right)^2 + \frac{1}{2}\left(\frac{u_{,\phi} + w}{R}\right)^2 \quad (6)$$

which is used in Chapter 3 as Eq.(3.10) and Eq.(4.3) in Brush and Almroth (1975).

Based on the following assumptions, we could derive the normal vector rotation and current principal centerline curvature for both straight segment and circular arc segment.

Assumption 1: The rotation angle β is very small,

Assumption 2: Bending deformation is dominant and stretching is negligible, namely,

$$u_{,s} \approx 0, \quad u_{,ss} \approx 0 \text{ or } \lambda_1 = \frac{ds}{dS} \approx 1.$$

2. Rotation of normal vector

We assumed the angle between the current normal vector \hat{n} and the S (arc length) is α ,

the angle between the current normal vector \hat{n} and normal vector \hat{N} at the reference is β .

$$\text{Then, we have } \beta + \frac{\pi}{2} = \alpha, \text{ and } \hat{n} \cdot \hat{A} = \cos \alpha = -\sin \beta \quad (7)$$

Substituting Eq.(2.16) into Eq.(7), we obtain:

$$\sin \beta = \frac{d}{\lambda_1} = \frac{w_{,s} + K_1 u}{\lambda_1} = \frac{w_{,s} + K_1 u}{\sqrt{(1 + u_{,s} - K_1 w)^2 + (w_{,s} + K_1 u)^2}} \quad (8)$$

For *straight line segment* ($K_1=0$), according to assumption 1, Eq.(8) becomes

$$\sin \beta \approx \beta = \frac{w_{,s}}{\sqrt{(1 + u_{,s})^2 + w_{,s}^2}} \quad (9)$$

According to assumption 2 and $w_{,s}^2 \ll 1$, Eq.(9) becomes: $\beta = w_{,s}$, for the coordinates shown in Figure 3.2, we have the normal vector rotation for straight segment

$$\beta = -w_{,s} \quad (10)$$

which is used in Chapter 3 as Eq.(3.1).

For *circular arc segment* ($K_1 \neq 0$), according to assumption 1 and 2, Eq.(8) becomes:

$$\beta = K_1 u + w_{,s} \text{ Since } dS = R d\phi \text{ and } K_1 = \frac{1}{R}, \text{ we obtain}$$

$$\beta = \frac{u + w_{,\phi}}{R} \quad (11)$$

For the coordinates shown in Figure 3.3, we have

$$\beta = \frac{u - w_{,\phi}}{R} \quad (12)$$

which is used in Chapter 3 as Eq.(3.7) and Eq.(4.4) in Brush and Almroth (1975).

3. The current principal centerline curvature

For *straight segment* ($K_1=0$), the centerline curvature at the current configuration, k_s , will be obtained from Eq.(2.20):

$$k_s = \frac{cd_{,s} - dc_{,s}}{\lambda_1^3} = \frac{(1 + u_{,s})w_{,ss} - w_{,s}u_{,ss}}{\lambda_1^3} \quad (13)$$

According to assumption 2 ($u_{,s} = u_{,ss} = 0$), $\lambda_1 \approx \sqrt{1 + w_{,s}^2}$, the Eq.(13) becomes:

$$k_s = \frac{w_{,ss}}{(1 + w_{,s}^2)^{\frac{3}{2}}} \quad (14)$$

which is used in Chapter 3 as Eq.(3.6).

For *circular arc segment*, it seems not easy to get the simplified curvature from Eq.(2.20). We begin from Eq.(12), which is based on the small rotation, however, for finite rotations, we use

$$\sin \beta = \frac{u - w_{,\phi}}{R} \quad (15)$$

According to Flugge (1973, pp.362), we have the change of curvature:

$$\kappa_{\phi} = \frac{\dot{\beta}}{R} \quad (16)$$

By differentiating Eq.(15), we obtain:

$$\dot{\beta} = \frac{u_{,\phi} - w_{,\phi\phi}}{R \cos \beta} \quad (17)$$

where

$$\cos \beta = \sqrt{1 - \sin^2 \beta} = \sqrt{1 - \left(\frac{u - w_{,\phi}}{R}\right)^2} \quad (18)$$

Substituting from Eqs.(17),(18) into Eq.(16), we have

$$\kappa_{\phi} = \frac{\frac{u_{\phi} - w_{,\phi\phi}}{R}}{R\sqrt{1 - \left(\frac{u - w_{,\phi}}{R}\right)^2}} \quad (19)$$

which is Eq.(11) in Corona and Pourboghra (1998) for small rotation case.

APPENDIX B

Here we try to prove the equivalence of two formulations in the pressure modeling, ie:

$$F_{Ext}^P = p \sum_{i=1}^I \int_{A^i} \hat{n}^i \frac{\partial(\Delta u^i)}{\partial \underline{c}} dA_p^i \approx -p \sum_{i=1}^I \int_{A^i} \frac{\partial(\Delta w^i)}{\partial \underline{c}} dA_p^i \quad (1)$$

From the Chapter 3 kinematics, for the point on mid-surface (circular segment), we have

$$\xi^i = Z_c + (R + w^i) \sin \bar{\phi} + v^i \cos \bar{\phi} \quad (2.a)$$

$$\eta^i = Y_c + (R + w^i) \cos \bar{\phi} - v^i \sin \bar{\phi} \quad (2.b)$$

where $\bar{\phi} = \phi_0 + \phi$. Replacing the w, u with w^i, v^i respectively from Eqs.(3.8a-b).

Define \hat{n}^i is the unit outward normal to the surface A_p^i , then we have

$$\hat{n}^i = \frac{\left(-\frac{\partial \xi^i}{\partial \phi}, \frac{\partial \eta^i}{\partial \phi}\right)}{\left\| \left(-\frac{\partial \xi^i}{\partial \phi}, \frac{\partial \eta^i}{\partial \phi}\right) \right\|} \quad (3)$$

where

$$-\frac{\partial \xi^i}{\partial \phi} = -\frac{\partial w^i}{\partial \phi} \sin \bar{\phi} - (R + w^i) \cos \bar{\phi} - \frac{\partial v^i}{\partial \phi} \cos \bar{\phi} + v^i \sin \bar{\phi} \quad (4.a)$$

$$\frac{\partial \eta^i}{\partial \phi} = \frac{\partial w^i}{\partial \phi} \cos \bar{\phi} - (R + w^i) \sin \bar{\phi} - \frac{\partial v^i}{\partial \phi} \sin \bar{\phi} - v^i \cos \bar{\phi} \quad (4.b)$$

$$\left\| \left(-\frac{\partial \xi^i}{\partial \phi}, \frac{\partial \eta^i}{\partial \phi}\right) \right\| = \left\{ \left(\frac{\partial w^i}{\partial \phi} - v^i\right)^2 + \left[(R + w^i) + \frac{\partial v^i}{\partial \phi}\right]^2 \right\}^{1/2} \approx R + w^i \quad (4.c)$$

We also have

$$\frac{\partial(\Delta u^i)}{\partial \underline{c}} = \left(\frac{\partial(\Delta \eta^i)}{\partial \underline{c}}, \frac{\partial(\Delta \xi^i)}{\partial \underline{c}} \right) \quad (5)$$

where

$$\Delta \xi^i = \Delta w^i \sin \bar{\phi} + \Delta v^i \cos \bar{\phi} \quad (6.a)$$

$$\Delta \eta^i = \Delta w^i \cos \bar{\phi} - \Delta v^i \sin \bar{\phi} \quad (6.b)$$

Combining (3), (4.a-c),(5) and (6.a-b), we have

$$\begin{aligned} \hat{n}^i \frac{\partial(\Delta u^i)}{\partial \underline{c}} &= -\frac{1}{R + w^i} \left((R + w^i) \frac{\partial(\Delta w^i)}{\partial \underline{c}} + v^i \frac{\partial(\Delta v^i)}{\partial \underline{c}} + \frac{\partial v^i}{\partial \phi} \frac{\partial(\Delta w^i)}{\partial \underline{c}} - \frac{\partial w^i}{\partial \phi} \frac{\partial(\Delta v^i)}{\partial \underline{c}} \right) \\ &\approx -\frac{\partial(\Delta w^i)}{\partial \underline{c}} \end{aligned} \quad (7)$$

For the straight segment, same expression can be obtained. Thus, we have proven the (1).

Since $\frac{\partial^2(\Delta w^i)}{\partial^2 \underline{c}} = 0$, there will be no stiffness matrix due to pressure going to left side

of Newton-Raphson expression.

REFERENCE

- Ahmetoglu M. and Altan T., 2000, Tube hydroforming: state-of-the-art and future trends, *J Mater Process Tech* 98: (1) 25-33.
- Anon, 1997, Hydroforming technology, *Advanced Material Process*, 151(5) ,50-53
- Bathe, K-J, 1982, *Finite Element Procedures in Engineering Analysis*. Prentice-Hall, New Jersey.
- Becker, R.C., 1992, An efficient semi-implicit integration algorithm for anisotropic flow potentials
- Brush, D.O. and Almroth, 1975, *Buckling of Bars, Plates, and shells*, McGraw-Hill.
- Choudhry, S. and Lee, J.K., 1994, Dynamic plane-strain finite element simulation of industrial sheet metal forming processes, *Int. J. Mech. Sci.* Vol.36, No. 3, pp.189-207.
- Corona, E. and Pourboghrat, F., 1998, *Bending-Stretch Forming of Extrusions- BETGES Computer Program Manual*, Alcoa internal report, March.
- Dohmann, F. and Hartl, Ch., 1997, Tube hydroforming: research and practical application, *J. Mater Process Tech* 71 174-186.
- Dohmann, F. and Hartl, Ch., 1996, Hydroforming: a method to manufacture light-weight parts, *J Mater Process Tech* 60 669-676.
- Flugge, W., 1973. *Stresses in Shells*, 2nd Edition. Springer-Verlag, New York.
- Germain, Y., Chung, K. and Wagoner, R.H., 1989, *Int. J. Mech. Sci.* Vol. 31, No1, pp. 1-24.
- Hibbitt, H. D., 1979, "Some follower forces and load stiffness", *Int. J. num. Mech. Engng*, 14, 937-941.
- Hsu, Tze-Chi and Chu, Chan-Hung, 1995, A finite element analysis of sheet metal forming process, *J Mater Process Tech* 54 , 70-75.
- Hu, P., Liu, Y.Q., Li, Y.X. and Lian, J., 1997, Rigid viscoplastic finite element of the gas-pressure constrained bulging of superplastic circular sheets into cone disk shape dies, *Int. J. Mech. Sci.* Vol. 39, No.4, pp. 487-496.
- Kobayashi, S., Oh, S.I and Altan, T., 1989, *Metal Forming and the Finite Element Method*, Oxford University Press, New York.
- Longhouse, B., 1998, Applied pressure sequence hydroforming, 3rd Annual automotive tube fabricating.

Marc's Theory and user information

Morphy, G., 1997, Hydroforming high strength steel tube for automotive structural applications using expansion, SAE International Congress & Exposition.

Nagtegaal, Joop C. and Rebelo, N., 1988, On the development of a general purpose finite element program for analysis of forming processes, Int. J. Num. Methods Eng., 25, 113-131.

Ni, C.M., 1994, Stamping and hydroforming process simulation with a 3D finite element code, SAE Paper #940753, SAE SP-1021

Noh, T.S. and Yang, D.Y., 1998, A general formulation for hydroforming of arbitrarily shaped boxes and its application to hydroforming of an elliptic-circular box, Journal of Manufacturing Science and Engineering, August, Vol. 120 481-488.

Oden, J.T. and Pires, E.B., 1983, Nonlocal and nonlinear friction laws and variational principles for contact problems in elasticity, ASME J. Appl. Mech., Vol. 50, 67-76.

Oh, S.I., 1982, Finite element analysis of metal forming processes with arbitrarily shaped dies, Int. J. Mech. Sci. Vol. 24, No. 8, pp. 479-493.

Pourboghrat, F., Karabin, M.E., Becker, R.C. and Chung, Kwansoo, 2000, "A hybrid membrane/shell method for calculating springback of anisotropic sheet metals undergoing axisymmetric loading", International Journal of Plasticity 16 677-700.

Sheet-S, Ohio State University

Siebert K., Haussermann M. and Losch B., et al, 2000, Recent developments in hydroforming technology, J Mater Process Tech 98: (2) 251-258.

The ABCs of Hydroforming, Vari-Form Inc.

Wang, N.M. and Tang, S.C., 1988, Analysis of bending effects in sheet forming operations, Int. J. Num. Methods Eng., 25 253-267.

Wang, N.M. and Budiansky, B., 1978, Analysis of sheet metal stamping by a finite element method, ASME J. Appl. Mech., Vol. 45 73-82.

Zhang, SH, 1999, Developments in hydroforming, J Mater Process Tech 91:(1-3) 236-244.

MICHIGAN STATE UNIVERSITY LIBRARIES



3 1293 02094 6970